

This is an Open Access document downloaded from ORCA, Cardiff University's institutional repository:<https://orca.cardiff.ac.uk/id/eprint/136155/>

This is the author's version of a work that was submitted to / accepted for publication.

Citation for final published version:

Sosdian, S. M. and Lear, C. H. 2020. Initiation of the western Pacific warm pool at the middle Miocene climate transition? *Paleoceanography and Paleoclimatology* 35 (12) , e2020PA003920.
10.1029/2020PA003920

Publishers page: <http://dx.doi.org/10.1029/2020PA003920>

Please note:

Changes made as a result of publishing processes such as copy-editing, formatting and page numbers may not be reflected in this version. For the definitive version of this publication, please refer to the published source. You are advised to consult the publisher's version if you wish to cite this paper.

This version is being made available in accordance with publisher policies. See <http://orca.cf.ac.uk/policies.html> for usage policies. Copyright and moral rights for publications made available in ORCA are retained by the copyright holders.



1 **Initiation of the Western Pacific Warm Pool at the Middle Miocene Climate Transition?**

2
3
4
5 **S.M. Sosdian* & C. H. Lear**

6 School of Earth and Ocean Sciences, Cardiff University, Main Building, Park Place, Cardiff,
7 CF10 3AT

8
9 *Corresponding author

10
11
12 **Abstract**

13
14 Across the middle Miocene, Earth's climate underwent a major cooling and expansion of the
15 Antarctic ice sheet. However, the associated response and development of the tropical climate
16 system is not fully understood, in part because this is influenced by both global climate and
17 also low latitude tectonic gateways and paleoceanography. Here we use combined $\delta^{18}\text{O}$ and
18 Mg/Ca of planktic foraminifera to reconstruct the thermal history and changes in hydrology
19 from the Indo-Pacific region from 16.5 to 11.5 Ma. During the warmth of the early middle
20 Miocene, our records indicate a dynamic ocean-atmosphere system in the Indo-Pacific region,
21 with episodes of saltier and warmer tropical surface waters associated with high pCO_2 and
22 retreat of the Antarctic ice sheet. We show that across the middle Miocene Climate Transition
23 (MMCT) surface ocean temperatures in the Indo-Pacific cooled by $\sim 2^\circ\text{C}$, synchronous with the
24 advance of the Antarctic ice sheet. The associated cooling in the Southern Ocean appears to have
25 started earlier, and was stronger. Further, we show that western Pacific Ocean warmed and
26 eastern tropical Indian Ocean freshened following the MMCT, likely caused by the constriction
27 of the Indonesian Seaway and reduced connectivity between the Pacific and Indian Oceans
28 following Antarctic glaciation. The MMCT therefore represented a key phase in the evolution
29 of the West Pacific Warm Pool and associated tropical climate dynamics.

30
31 **Keywords:** Miocene, Tropics, Mg/Ca, planktic foraminifera, glaciation, Indo-Pacific

32
33 **Key Points:**

- 34
- 35 • Low latitude Indo-Pacific sea surface temperatures cooled synchronous with
36 the advance of the Antarctic ice sheet
 - 37 • Eastern Tropical Indian Ocean freshened following the Middle Miocene Climate
38 Transition
 - 39 • Sea level fall and changing paleogeographic conditions constricted the
40 Indonesian Seaway modifying the Tropical Indian Ocean climate and
41 warming the western Pacific ocean.
- 42
43

44 For resubmission to *Paleoceanography, Special Issue on the Miocene*

45
46
47
48
49
50
51
52
53
54
55

56 **1. Introduction & Background**

57 Across the Middle Miocene, the Earth's climate gradually changed from a period of global
58 warmth and retreat of the Antarctic ice sheet known as the Miocene Climatic Optimum
59 (MCO; ~17-14.7 Ma) to a cooler climate with regrowth of the Antarctic ice sheet at the
60 Middle Miocene Climate Transition (MMCT), exhibited by an stepwise increase in the
61 benthic foraminiferal oxygen isotope record (14.2-13.9 Ma). Global warmth and high carbon
62 dioxide (CO₂) levels were pervasive during the MCO, with global surface temperature
63 perhaps > 7°C than present (Shevenell et al., 2004; Lewis et al., 2007; Verducci et al., 2007;
64 Kuhnert et al., 2009; Majewski & Bohaty, 2010; Levy et al., 2016; Super et al., 2018;
65 Hartman et al., 2018; Sangiorgi et al., 2018). Following the MCO, CO₂ decreased from ~580-
66 670 ppm to 380-420 ppm, and the Antarctic ice sheet re-advanced, causing a sea level fall of
67 several tens of metres (Lear et al., 2010, John et al., 2011; Foster et al., 2012, Badger et al.,
68 2013; Sosdian et al., 2018). Understanding the driving mechanisms of this major step in
69 Earth's climate evolution where the Antarctic ice sheet transitioned from a wet-based to dry
70 based ice sheet (i.e. more modern like ice sheets) (Lewis et al., 2007) is critical to understand
71 the interactions between carbon cycle, cryosphere and climate change. Existing records
72 demonstrate large scale cooling in regions proximal to Antarctica and the North Atlantic
73 (Shevenell et al., 2004; Lewis et al., 2007; Verducci et al., 2007; Kuhnert et al., 2009;
74 Majewski & Bohaty, 2010; Levy et al., 2016; Super et al., 2018; Hartman et al., 2018;
75 Sangiorgi et al., 2018), reorganization of polar frontal systems (Verducci et al., 2007; Kuhnert
76 et al., 2009), and intensification of equatorial upwelling and overturning circulation
77 (Holbourn et al., 2013; 2014). For example, the continuous, orbitally-resolved Mg/Ca-sea
78 surface temperature (SST) and planktic isotope record from the Pacific sector of the Southern
79 Ocean shows a 6 to 7°C cooling and freshening preceding the main glaciation step by 300 kyr
80 (Shevenell et al., 2004), although non-thermal effects (e.g., pH, dissolved inorganic carbon)
81 on Mg/Ca must be considered and warrant caution when interpreting the nature and extent of
82 cooling (Gray & Evans, 2019; Holland et al., 2020). The timing of these changes has led to
83 the idea that meridional heat/moisture transport and an early thermal isolation of the Antarctic
84 continent played a fundamental role in triggering ice growth (Shevenell et al., 2004). Recent
85 Antarctic ice-proximal reconstructions (e.g., Sangiorgi et al., 2018) have shown sea ice
86 expansion, increasing SST gradients and cooling of ice-proximal surface waters across the
87 MMCT hinting at a northward shift in the Southern Ocean frontal system. As most SST
88 records are derived from circum-polar regions, it is difficult to determine the global climatic
89 signature of the MMCT and identify the role of Southern Ocean processes, carbon cycle, or
90 oceanographic changes (Shevenell et al., 2004; Verducci et al., 2007; Kuhnert et al., 2009;
91 Super et al., 2018; Sangiorgi et al., 2018). Records from both high and low latitude sites are

92 necessary to mechanistically understand the cause and effects of this key climate transition
93 and test proposed hypotheses.

94 The middle Miocene also witnessed important changes in the tectonic configuration
95 of low latitude ocean seaways, which must be considered when interpreting records of
96 tropical sea surface temperature and hydrology. Low latitude tectonic events (e.g.
97 Panamanian and Indonesian Seaway constriction) could affect the distribution of heat
98 between ocean basins and reorganize tropical surface ocean structure and climate patterns
99 (Gourlan et al., 2008; von der Heydt & Dijkstra, 2011; Hamon et al., 2013; Bialik et al., 2019).
100 In the present day, the Indonesian Throughflow transports the warm waters of the Western
101 Pacific Warm Pool (WPWP) and excess heat and freshwater through a series of straits and
102 shallow seas eventually entering and warming the Indian Ocean. This heat export affects
103 ocean-atmosphere coupling in the tropical Pacific and Indian Oceans with implications for the
104 development of Indian Ocean Dipole events and changes in global atmospheric circulation
105 patterns (Schneider, 1998; Wajsovicz and Schneider, 2001; Sprintall, 2003).

106 On geological timescales the long-term drift of Australia towards Asia has
107 progressively changed the structure of this seaway. From the late Oligocene to the early
108 Miocene, the Indonesian seaway became a shallow water throughflow effective for surface
109 water transport while the transport of deep water between the deep oceans diminished (Kuhnt
110 et al., 2004). Early biogeographic studies of discrete time slices (22, 16, 8 Ma) suggested
111 tectonic closure of the Indonesian seaway as a trigger for invigoration of tropical surface
112 ocean circulation systems in the middle Miocene (Kennett et al., 1985), although tectonic
113 reconstructions suggest that the Indonesian seaway became restricted before the middle
114 Miocene (Ali et al., 1994; Hall, 1996; 2002). Further, the deeper and more open Indonesian
115 seaway could impact the position of the WPWP, with a Miocene warm pool residing in the
116 eastern Indian Ocean (von der Hedyt & Dijkstra, 2011). This suggests a pivotal role for the
117 seaway in setting the climate budget of the Indo-Pacific region, proximal seas and distal
118 outflow locations in the Miocene Tropical Indian Ocean.

119
120 To unravel the relative roles of paleogeography, CO₂, and glaciation in middle Miocene
121 climate, equatorial surface ocean temperature records are required. However, documentation
122 of low-latitude conditions is limited both spatially and temporally, and a deeper understanding
123 awaits development of records comparable to those available from the Southern Ocean.
124 Oxygen isotope records from the equatorial Pacific region show a warming across the middle
125 Miocene, however confident interpretation of these records is difficult due to likely diagenetic
126 overprints (Savin et al. 1985; Stewart et al. 2004). Orbital scale Mg/Ca-derived sea surface
127 temperature (SST) and oxygen isotope ($\delta^{18}\text{O}$) records from the South China Sea (SCS) show

128 dynamic changes in tropical hydrology (i.e. warming and freshening) in response to Antarctic
129 glaciation suggesting a role for large shifts in the Intertropical Convergence Zone (ITCZ)
130 position (Holbourn et al. 2010). In contrast, low resolution alkenone-derived SST
131 reconstructions from the Eastern Equatorial Pacific (EEP) shows a cooling event across the
132 MMCT (Rousselle et al. 2013), although this record is difficult to interpret due to proxy
133 saturation during the warm MCO, prior to the MMCT. In the eastern tropical Indian Ocean,
134 Sosdian et al. (2020) show that SSTs in this region cooled along with the MMCT. These lines
135 of evidence suggest that the MMCT was associated with a climate reorganization event in the
136 low latitudes, however, additional records are needed to resolve the roles of CO₂, glaciation,
137 and paleogeography in context of tropical climate evolution.

138

139 Here we present records of surface ocean hydrographic conditions derived from combined
140 planktic foraminiferal Mg/Ca and oxygen isotope ($\delta^{18}\text{O}_p$) data from Ocean Drilling Program
141 (ODP) Site 806 located in the western equatorial Pacific Ocean and $\delta^{18}\text{O}_p$ record from ODP
142 Site 761 from the eastern tropical Indian Ocean. The climate records span the time period
143 from 16.5 to 11.5 Ma and allow us to explore regional versus global changes in climate. We
144 further use the combined Mg/Ca and $\delta^{18}\text{O}_p$ from surface dwelling planktic foraminifera to
145 reconstruct the oxygen isotope composition of seawater ($\delta^{18}\text{O}_{sw}$) in order to evaluate temporal
146 changes in tropical surface ocean salinity across the middle Miocene. Overall we find that the
147 Indo-Pacific cooled across the MMCT in step with Antarctic glaciation. Further, we show that
148 the Indian Ocean freshened relative to the Pacific and western equatorial Pacific warmed
149 following this transition likely caused by the constriction of the Indonesian Seaway. The
150 Middle Miocene Climate Transition therefore likely represented a key phase in the evolution
151 of the West Pacific Warm Pool and associated tropical climate dynamics.

152

153 **2. Materials & Methods**

154 **2.1 Age models and oceanographic settings of study sites**

155 **2.1.1 ODP Site 806B – western equatorial Pacific Ocean**

156 Ocean Drilling Program (ODP) Site 806B (2520 m water depth, 0°19.1'N, 159°21.7'E; Fig.
157 1) is located on the Ontong Java Plateau in the western equatorial Pacific and has relatively
158 high sedimentation rates (20-30 m/Myr) with a complete Miocene section of carbonate ooze.
159 A 5° latitudinal northward drift of the Ontong Java Plateau since the Middle Miocene puts
160 this site in a tropical location during the present day (~5°S; Figure S1). This study uses
161 sediment samples from cores 43 to 60 (400–566 metres below seafloor (mbsf)), with a
162 temporal resolution of ~130 kyr during the study interval (16.5 to 11.5 Ma). We use the age
163 model of Lear et al., (2015) which is a fourth order polynomial fit through nannofossil and

164 planktic foraminiferal biostratigraphical events at ODP 806B on the Berggren et al., (1995)
165 timescale for new planktic Mg/Ca presented here and previously published oxygen isotope
166 records (Corfield & Cartlidge, 1993; Nathan & Leckie, 2009; Lear et al., 2015). The benthic
167 oxygen isotope ($\delta^{18}\text{O}_b$) data from Holbourn et al. (2013) are presented on the Lear et al.,
168 (2015) age model.

169
170 ODP Site 806 is today located in the warm waters of the WPWP, due to the buildup of warm
171 waters trapped in front of the Indonesian archipelago (Figure 1). Here, the modern day
172 thermocline is deep and surface waters exceed 29°C, with a small range of ~29- 29.5°C. Since
173 at least the early Miocene, ODP Site 806 has remained in western Pacific equatorial waters
174 (Sclater et al., 1985). On interannual timescales, the El Niño Southern Oscillation shoals the
175 thermocline and lessens the precipitation in the WPWP. Due to its location, good core
176 recovery, and preservation of microfossils, ODP Site 806 is an ideal location to examine the
177 thermal stability over wide range of timescales (i.e. kyr-Myr) of the western equatorial Pacific
178 region.

181 **2.1.2 ODP Site 761B – eastern tropical Indian Ocean**

182 ODP Site 761 was cored in 2179 m water depth on the Wombat Plateau, off northwest
183 Australia (16° 44.23' S, 115° 32.10' E ; Fig. 1). A 10-15° latitudinal northward drift of
184 Australia since the Middle Miocene puts this site in a subtropical to tropical location during
185 the present day (~21°S; Scotese et al., 1988; Figure S1). The continuously cored Neogene
186 section studied here extends between 35 and 50 mbsf and slow sedimentation rates have led to
187 unusually shallow burial depths (<50 m) for the middle Miocene sequence, leading to
188 enhanced foraminiferal preservation. 20 cc sediment samples were taken at approximately 10
189 cm resolution, resulting in average temporal resolution of ~23 kyr for planktic foraminiferal
190 stable isotopes. Previously published benthic foraminiferal stable isotope and planktic
191 foraminiferal Mg/Ca data exist at this site with an average temporal resolution of 17 and 23
192 kyr respectively (Holbourn et al., 2004; Lear et al., 2010; Sossian et al., 2020). We use the
193 age model of Lear et al., (2010) which is a fourth order polynomial fit through the
194 biostratigraphic and isotopic datums provided by Holbourn et al. (2004) on the Berggren et
195 al. (1995) timescale. Surface salinity estimates from nearby sites are 34.5 (GLODAP; Key et
196 al., 2004).

197
198
199

200 ODP Site 761 sits in the midst of a dynamic hydrographic regime in the eastern Indian Ocean.
201 During the austral winter, a subtropical high occupies the site and dry easterly winds blow
202 over the Australian continent and into the Indian Ocean. During the austral summer, the
203 subtropical high moves poleward and the ITCZ penetrates further south delivering monsoonal
204 rain. Seasonal temperatures range from 30.9°C in the austral summer to 25.3°C in the austral
205 winter with mean annual temperatures around 28°C. Since the middle Miocene, it has been
206 proximal to the western edge of the present day Indonesian throughflow, which transports
207 cool, low salinity North Pacific thermocline water to the Indian Ocean. Additionally it is
208 directly under the influence of the modern Leeuwin Current, a narrow, shallow current that
209 transports warm, low-salinity, nutrient-deficient water southward along the west coast of
210 Australia (Pattiaratchi, 2009; Gallagher et al., 2009), derived from water formed within the
211 Indonesian Throughflow and the Central Indian Ocean (Wijffels et al., 2002; Domingues et
212 al., 2007). Surface salinity estimates from nearby sites are 34.15 (GLODAP; Key et al.,
213 2004).

214

215 **2.2 Mg/Ca and $\delta^{18}\text{O}$ Analysis**

216 Between 20-30 tests of planktic foraminifera *Dentoglobigerina altispira* and 30-40
217 tests of the planktic foraminifera *Trilobatus trilobus* were picked from the 300-355 μm size
218 fraction at ODP Sites 806 and 761, respectively. The picked specimens were weighed and
219 crushed between plates and homogenized for analysis. In some samples (~25 out of 229
220 samples), where planktic foraminifera abundance was low, fewer specimens (10-20
221 individuals) were analyzed. The Mg/Ca and $\delta^{18}\text{O}_p$ data were generated from splits of the same
222 samples after initial homogenization of crushed tests. Mg/Ca data for ODP Site 761 were
223 previously published in Sosdian et al., (2020), in this study we also present the $\delta^{18}\text{O}_p$ data
224 from the same samples.

225 Test fragments for Mg/Ca analyses were cleaned using a protocol to remove clays
226 and organic matter (Barker et al., 2003). Between the clay removal and oxidative steps the
227 samples were examined under a binocular microscope, and non-carbonate particles were
228 removed using a fine paintbrush. Samples were dissolved in trace metal pure 0.065M HNO_3
229 and diluted with trace metal pure 0.5M HNO_3 to a final volume of 350 μl . Samples were
230 analyzed at Cardiff University on a Thermo Element XR ICP-MS against standards with
231 matched calcium concentration to reduce matrix effects (Lear et al., 2002). Mg/Ca data for a
232 sample was rejected when Al/Ca exceeded 80 $\mu\text{mol/mol}$ and/or $\text{Fe/Mg} > 1$. Cleaning
233 effectiveness was supported by uncorrelated Mg/Ca, Fe/Ca, and Mn/Ca. Long term precision
234 as determined by analyzing an independent consistency standard during each run for one year
235 is $\sim 0.5\%$ (r.s.d.) for Mg/Ca.

236 Stable oxygen and carbon isotope ratios were measured at Cardiff University on a
237 Finnigan MAT 252 micro-mass spectrometer Kiel III Carbonate Device when sample weights
238 were less than 100 µg and measured on a Delta isotope ratio mass spectrometer when samples
239 were greater than 100 µg. Analytical errors based on replicate measurements of a laboratory
240 standard (NBS 19) are 0.08‰ for $\delta^{18}\text{O}$ (2σ).

241

242 **2.4 Planktic Foraminiferal Taxonomy and Ecology**

243 At ODP Site 806, the abundant *D. altispira* is an ideal species to reconstruct SST in
244 the western equatorial Pacific as it is a near-surface dweller, and common in tropical waters
245 (Fig. S2; Corfield & Cartlidge, 1992). *D. altispira* evolved in the late Oligocene and became
246 extinct in the late Pliocene (Kennett & Srinivasan, 1983 Gasperi & Kennett, 1992, 1993;
247 Chaisson & Leckie, 1993; Norris et al. 1993). Comparison of isotope records of a typical
248 planktic foraminiferal assemblage in the western equatorial Pacific shows that *D. altispira*
249 behaves as a shallow water species for the middle Miocene, and probably harbors symbionts
250 similar to contemporaneous *T. trilobus* (Pearson, 1995).

251

252 In the modern ocean, *T. trilobus* is considered to be a morphospecies of *T. sacculifer*,
253 although *T. sacculifer* did not evolve until the Pliocene (Figure S2; Kennett & Srinivasan,
254 1983; Spezzaferri et al., 2015). *T. trilobus*, a multi-chambered and symbiont-bearing species,
255 is predominantly a mixed layer dweller calcifying at 0-50m and is abundant in subtropical to
256 tropical oceans. Numerous studies have successfully used this foraminiferal species to study
257 low latitude surface processes in the Quaternary and Neogene time periods (e.g., Elderfield &
258 Ganssen, 2000; Wara et al., 2005; Badger et al., 2013). At ODP Site 761, *T. trilobus* is
259 abundant throughout the middle Miocene and thus is an ideal species to estimate SSTs
260 (Zachariasse, 1992). Studies have shown that temperatures derived from *T. sacculifer* are
261 most suitable for estimating annual mean SST in tropical waters, between 20° N/S within
262 $\pm 1^\circ\text{C}$ (Anand et al., 2003; Fraile et al., 2009; Sosdian et al., 2020).

263

264 **2.5 Mg/Ca-paleotemperature relationship and non-thermal influences**

265 Test Mg/Ca and calcification temperature in planktic foraminifera show an exponential
266 relationship across a range of modern day surface ocean temperatures deduced from core-top,
267 culturing and sediment trap studies (Dekens et al., 2002; Anand et al., 2003; Duenas-
268 Bohorquez et al., 2011). The exponential constant that describes the temperature sensitivity
269 (A in equation 1) ranges from 0.070 to 0.113 determined from a wide range of modern
270 planktic species (Elderfield and Ganssen, 2000; Rosenthal and Lohmann, 2002; Anand et al.,
271 2003; Cleroux et al., 2008; Regenberg et al., 2009).

272 $Mg/Ca_{foram} = Be^{AT}$ (eq. 1)

273 Accurate reconstructions of Miocene sea surface temperatures derived from planktic Mg/Ca
 274 ratios requires consideration of variations in seawater Mg/Ca.

275
$$\frac{Mg}{Ca_{foram}} = \left[\frac{\frac{Mg}{Ca_{sw}}(t)}{\frac{Mg}{Ca_{sw}}(0)} \right]^C Be^{AT} \quad (\text{eq. 2})$$

276 where $Mg/Ca_{sw}(t)$ and $Mg/Ca_{sw}(0)$ are seawater Mg/Ca ratios for the Miocene and present
 277 respectively and A, B, and C are constants (A=exponential, B=pre-exponential, C=power law
 278 constant). Mg and Ca have relatively long residence times (~13 Myr and ~1 Myr
 279 respectively) in the ocean (Broecker and Peng, 1982). Changes in weathering, hydrothermal
 280 activity, and carbonate deposition could lead to secular changes in Mg/Ca_{sw} . Seawater Mg/Ca
 281 values are independently estimated from a range of proxies (fluid inclusions, calcite veins,
 282 echinoderm, paired Mg/Ca-clumped isotope measurements of benthic foraminifera, fossil
 283 corals) (Dickson, 2002; Horita et al., 2002; Coggon, 2010; Rausch et al., 2013; Brennan et al.,
 284 2013;Gothmann et al., 2015; Evans et al., 2018). The modern day seawater Mg/Ca value is
 285 5.2 mol/mol (Broecker & Peng, 1982) and Miocene estimates derived from proxy data show
 286 an increase from 30 Ma to modern day. Several studies have used modelling to explore
 287 variations in Mg/Ca_{sw} with predictions for Mg/Ca_{sw} derived from pore water modelling data
 288 for the past 20 Myr (Fantle & DePaolo, 2006; hereafter FD06) and 40 Myr (Higgins &
 289 Schrag, 2012; hereafter HS12). Given the residence time of Mg and Ca, these models exhibit
 290 potentially short-term changes in Mg/Ca_{sw} and further predicts a large and rapid increase in
 291 Mg/Ca seawater over the Neogene, with considerable uncertainty in the input parameters
 292 (Figure S3). The estimated SSTs for ODP Site 761 show a large divergence particularly
 293 between the HS12 SST scenarios and others, with $SST > 35^\circ C$ in the MCO. Overall, we
 294 prefer the proxy data compilation as it derived from range of disparate proxies which
 295 converge to show a consistent increase in Mg/Ca_{sw} (Figure S4). Note we do not include the
 296 fossil coral data from Gothmann et al., (2015) data as it contains a considerable amount of
 297 variability. Thus, to account for changes in Mg/Ca_{sw} we fit a 4th order polynomial curve fit
 298 (eq. 3) through compiled Mg/Ca_{sw} proxy records to account for the changes in Cenozoic
 299 Mg/Ca_{sw} (eq. 3; Figure S5) including those derived from calcite veins (Coggon et al., 2010;
 300 Rausch et al., 2013), fluid inclusions (Horita et al., 2002; Brennan et al., 2013), echinoderms
 301 (Dickson et al., 2002), and larger benthic foraminifera (Evans et al., 2018).

302

303
$$seawater \frac{Mg}{Ca} = 5.3 - (0.153 * Age) + (0.00257 * Age^2) - (1.88e^{-5} * Age^3)$$

 304
$$+ (4.85e^{-8} * Age^4)$$

 305
$$(\text{eq. 3})$$

306 In addition to variations in seawater Mg/Ca, when converting planktic Mg/Ca into
307 temperature there must be consideration of non-thermal influences on shell Mg/Ca such as
308 changes in salinity and the carbonate system. Studies have shown a positive relationship
309 between salinity and shell Mg/Ca for some species (*G. ruber*, *O. universa*, *T. sacculifer*) with
310 a sensitivity of ~4 to 5% per PSU (Kisakurek et al., 2008; Duenas-Bohorquez et al., 2009;
311 Honisch et al., 2013). Further, Gray and Evans (2019) demonstrated that changes in pH
312 influences shell Mg/Ca with a -7.3% per increase in 0.1 pH unit and proposed a multi-variable
313 temperature calibration. However, their work shows that pH sensitivity is observed in some
314 species (e.g., *O. universa*, *G. ruber*, and *G. bulloides*) and not others (e.g., *T. sacculifer*).
315 Building on this carbonate system control, Holland et al., (2020) suggest that not pH but
316 changes in dissolved inorganic carbon (DIC) drive variations in *O. universa* Mg/Ca, with an
317 increase in DIC corresponding to an increase in Mg/Ca, however further work is needed to
318 explore the possible DIC sensitivity across a range of species.

319
320 Here we present a new planktic record based on *D. altispira* Mg/Ca (near surface dweller,
321 symbiont bearing) and revisit the Mg/Ca record derived from planktic *T. trilobus* (mixed layer
322 dweller, symbiont bearing) previously published by Sosdian et al., (2020) (Figure S6; S7)
323 across the middle Miocene. Available records of the carbonate system across the middle
324 Miocene suggest changes in the surface ocean pH and carbon reservoir (Foster et al., 2012;
325 Badger et al., 2013; Greenop et al., 2014; Sosdian et al., 2018; Sosdian et al., 2020) and we
326 consider these below when estimating SST. There is limited information on salinity
327 variations in the Indo-Pacific across the middle Miocene (Holbourn et al., 2010), but we
328 conduct a sensitivity analysis to consider these possible changes.

329
330 We calculate paleotemperatures from both records with consideration of the factors described
331 above. *D. altispira* is an extinct species and does not have a modern taxa equivalent.
332 However, the *D. altispira* Mg/Ca variations are similar to those from other modern planktic
333 taxa. For example, the range of Miocene Mg/Ca values (mean=3.6, max=3.9, min=3.3
334 mmol/mol) is similar to *G. ruber*, *T. trilobus*, and *G. bulloides* Mg/Ca values (mean=3.6,
335 max=4.7, min=1.7 mmol/mol) (this study; Kuhnert et al., 2009; Tripathi et al., 2009). Thus, to
336 estimate the calcification temperature from *D. altispira* Mg/Ca, we assume that this species
337 incorporates Mg into its calcite lattice similarly to modern taxa. However, across the middle
338 Miocene, a boron isotope derived pH compilation shows an increase of 0.1 pH units (Fig. 2A)
339 (Sosdian et al., 2018). As *D. altispira* is an extant species, accounting for changes in the
340 carbon system and its influences is not straightforward, as some modern species are
341 insensitive to pH changes (Gray & Evans, 2019). Here we apply the multi-species Mg/Ca-pH

342 correction from Evans et al., (2016) to assess the impact of middle Miocene pH increase on
343 Mg/Ca ratios and the SST reconstruction

$$344 \text{Mg/Ca}_{\text{CORRECTED}} = (1 - (8.05 - \text{pH}) \times 0.70 \pm 0.18) \times \text{Mg/Ca}_{\text{MEASURED}}. \text{ (eq. 4)}$$

345 For pH we use the interpolated pH estimates from Sossian et al., (2018). Briefly, a smoothed
346 trendline was fitted through the ‘G17’ pH scenario and interpolated at the sampling resolution
347 of the *D. altispira* Mg/Ca dataset.

348 Due to the lack of site specific records documenting salinity variations across the middle
349 Miocene, we perform a sensitivity analysis assuming modern, +1 PSU above modern, and -1
350 PSU below modern. We apply the multi-species Mg/Ca-salinity correction from Hollis et al.,
351 (2019) to explore the impact of middle Miocene salinity changes.

$$352 \text{Mg/Ca}_{\text{CORRECTED}} = (1 - (\text{salinity} - 35) \times 0.042 \pm 0.008) \times \text{Mg/Ca}_{\text{MEASURED}} \text{ (eq. 5)}$$

353 We convert *D. altispira* Mg/Ca to SST using the multi-species equation of Anand et al.,
354 (2003) which has an exponential constant A=0.09 and pre-exponential constant B=0.38. The
355 temperature equation is as follows:

356

$$357 \frac{\text{Mg}}{\text{Ca}_{\text{foram}}} = \frac{\frac{\text{Mg}}{\text{Ca}_{\text{sw}}}(t)^{0.41}}{\frac{\text{Mg}}{\text{Ca}_{\text{sw}}}(0)} 0.38e^{0.09T} \text{ (eq. 6)}$$

358

359

360 Where Miocene Mg/Ca_{sw} (t) is estimated using eq. 3 (this study). In previous studies, a linear
361 relationship between Mg/Ca_{foram} and Mg/Ca_{sw} was assumed (Lear et al., 2000). However it
362 has since been shown that a power function best describes this relationship (Hasiuk &
363 Lohmann, 2010; Lear et al., 2015). Here we use the power law constant of C=0.41, similar
364 to the value applied for *T. trilobus*, a symbiont-bearing, mixed layer dweller (Delaney et al.,
365 1985; Evans and Müller 2012).

366

367 Converting *T. trilobus* Mg/Ca ratios in SSTs is more straightforward, as thermal and non-
368 thermal influences on *T. sacculifer* Mg/Ca are better constrained. Gray and Evans (2019)
369 showed that *T. sacculifer* Mg/Ca is insensitive to pH change but sensitive to salinity changes.
370 Previously, mean annual SSTs were calculated for *T. trilobus* in Sossian et al., (2020), using
371 the *T. sacculifer* calibration without sac from Anand et al., (2003) where A=0.09, B=0.347
372 after accounting for seawater Mg/Ca assuming a power constant of C= 0.41 as determined by

373 Evans and Müller (2012) based on the data of Delaney et al., (1985). Those authors assumed
374 a constant value of 3.43 mol/mol for seawater Mg/Ca derived from fluid inclusion data
375 (Horita et al., 2002) for the duration of the record. Here we modify the approach of Sosdian
376 et al., (2020) to incorporate varying seawater Mg/Ca as set out in this study for $\frac{Mg}{Ca_{sw}}(t)$ term
377 in the paleotemperature calculation (eq. 3; Figure S5; Fig. 2B). Further we consider it more
378 appropriate to use the species-specific equation of Gray and Evans (2019) which takes into
379 account changes in temperature and salinity to estimate SST (eq.7).

380

$$381 \text{Mg/Ca} = \exp(a(S-35) + bT + c(\text{pH}-8) + d). \quad (\text{eq. 7})$$

382

383 Where $a=0.054$, $b=0.063$, $c=0.01$, and $d=-0.24$. Due to the lack of site specific records
384 documenting salinity variations across the middle Miocene in the Indian Ocean, we perform a
385 sensitivity analysis assuming modern, +1 PSU above modern, and -1 PSU below modern
386 salinity, similar to the analysis for ODP site 806.

387

388 To compare these tropical SST records to the high latitudes, we include the orbitally resolved
389 Southern Ocean *G. bulloides* Mg/Ca record from ODP Site 1171 (Shevenell et al., 2004).
390 Shevenell et al., (2004) converted *G. bulloides* Mg/Ca to SST using the Mg/Ca-SST
391 temperature equation from Mashiotta et al., (1999) and assumed modern Mg/Ca_{sw} . Here, to
392 ensure consistency amongst the comparisons, we recalculate SST from this Mg/Ca record
393 using the Gray and Evans (2019) multi-variable regression (eq. 7) for *G. bulloides* Mg/Ca,
394 where $a=0.036$, $b=0.064$, $c=-0.88$, and $d=0.15$ which takes into account temperature, pH, and
395 salinity. We use the interpolated pH record (Figure 2A) and the polynomial regression (eq. 3)
396 to estimate Mg/Ca seawater variations through the interval, and a C value of 0.72 (eq. 2) based
397 on calibration data (Evans et al., 2016). Due to the lack of site specific records documenting
398 salinity variations across the middle Miocene in the Southern Ocean, we perform a sensitivity
399 analysis assuming modern (34.5), +1 PSU above modern, and -1 PSU below modern salinity,
400 similar to ODP Sites 806 and 761.

401 In section 3.1 we present the planktic Mg/Ca records from ODP Sites 806 and 761 across the
402 middle Miocene and highlight the main their main features. In section 3.2 we consider the
403 thermal and non-thermal influences on these records and implications for interpretation and
404 uncertainties associated with the SST and planktic oxygen isotope records and paleoclimatic
405 variations.

406

407 2.6 Foraminiferal Preservation

408 Diagenesis alters the elemental composition of the test via partial dissolution,
409 overgrowths, or recrystallization, and thus burial conditions and preservation of the calcite
410 test need to be considered (Edgar et al., 2015). Partial dissolution in the water column or at
411 the seafloor selectively removes Mg^{2+} from the foraminiferal test (Rosenthal and Lohmann,
412 2002; Dekens et al., 2002; Regenberg et al., 2006). This dissolution effect is critical at
413 carbonate saturation values below 20 $\mu\text{mol/kg}$, as defined from core-top studies. Calcite
414 dissolution decreases Mg/Ca and increases $\delta^{18}\text{O}_p$, acting to bias both toward cooler values.
415
416 ODP Site 806 lies well above the modern lysocline and was above it during the middle
417 Miocene. SEM images of *D. altispira* from ODP Site 806 show original microstructure with
418 minimal infilling and dissolution indicators (Figure S2). However, although ODP Site 806 is
419 above the lysocline, modern carbonate saturation (ΔCO_3^{2-}) values are on average 10 $\mu\text{mol/kg}$
420 (data from WOCE cruise P10, station 10, Lewis and Wallace, 1998). Regenberg et al., (2006)
421 showed that the critical threshold values for which Mg^{2+} loss initiates is 20 $\mu\text{mol/kg}$ and thus
422 ideally Mg/Ca values should be corrected for dissolution. However, the species-specific
423 equation established from core-tops in the Regenberg et al., (2006) study and others (Dekens
424 et al., 2002; Rosenthal and Lohmann 2002) is not applicable to *D. altispira* as it is an extinct
425 species. Here we compare the Mg/Ca and $\delta^{18}\text{O}_p$ records with dissolution indicators to assess
426 whether temporal changes in calcite preservation could affect the interpretation of
427 paleoclimate records at ODP Site 806. Potential dissolution indicators, such as percent coarse
428 fraction (%CF) and average shell weight do not covary with Mg/Ca or $\delta^{18}\text{O}_p$ ($R^2 < 0.2$; Figure
429 S6). This suggests minor effects of dissolution on these records and moving forward we
430 assume that the overall changes in Mg/Ca and $\delta^{18}\text{O}_p$ at ODP Site 806 are related to climatic
431 signals.

432 Several lines of evidence suggest that dissolution does not significantly affect the
433 $\delta^{18}\text{O}_p$ or Mg/Ca values at ODP Site 761 as well. ODP Site 761 is situated well above the
434 modern lysocline, above the critical 20 $\mu\text{mol/kg}$ ΔCO_3^{2-} , in a relatively shallow burial depth
435 during the middle Miocene (<50 m). Visual examination (Figure S2) of *T. trilobus* from ODP
436 Site 761 shows moderately good preservation with no visible signs of infilling or dissolution.
437 Average shell weight of *T. trilobus*, from the 300-355 μm size fraction does not covary
438 ($R^2=0.20$) with the $\delta^{18}\text{O}_p$ or Mg/Ca record, supporting our argument that these values are not
439 biased (Figure S7).

440 Despite the reasonable appearance of foraminifera from both sites, all tests appear
441 frosty or opaque in contrast to exceptionally well preserved translucent test shells from
442 hemipelagic muds (Pearson et al., 2001). However, this preservation state is typical of most

443 deep-sea carbonates and is caused by micro-recrystallization of calcite. Diagenesis likely
444 affected the absolute $\delta^{18}\text{O}_p$ values, however large scale textural changes caused by
445 recrystallization are not evident in SEM images (Figure S2) suggesting that diagenesis did not
446 drive prominent shifts in $\delta^{18}\text{O}_p$. Additionally, Sr/Ca ratios from both cores show relatively
447 high values (~1.1-1.2 mmol/mol) that are consistent across much of the record suggesting that
448 diagenesis did not have a major influence on the variations of Mg/Ca and $\delta^{18}\text{O}_p$. Furthermore,
449 Sexton et al., (2006) showed that Mg/Ca values decrease by a negligible amount with initial
450 diagenetic alteration, thus temporal changes in Mg/Ca are less likely to be affected. For the
451 reasons outlined above we believe that diagenesis had a minimal effect on our records and we
452 therefore interpret the geochemical records in terms of changing paleoceanographic
453 conditions and interpret relative changes in SST rather than absolute SSTs.

454

455 **2.7 Calculation of surface seawater $\delta^{18}\text{O}$**

456 To assess changes in surface ocean evaporation and precipitation changes in the Indo-
457 Pacific region we use combined measurements of $\delta^{18}\text{O}_p$ and Mg/Ca from surface dwelling
458 foraminifera, *D. altispira* and *T. trilobus* (Fig. 2C; Figure S6, S7). The foraminiferal $\delta^{18}\text{O}_p$
459 signal is dependent upon SST, salinity, and ice volume, whereas the Mg/Ca signal is primarily
460 a temperature signal. Here we calculate planktic $\delta^{18}\text{O}_{sw}$ using the following equation (8) from
461 Bemis et al., (1998):

$$462 \quad \delta^{18}\text{O}_{sw}(V - SMOW) = 0.27 + \frac{((T(^{\circ}\text{C})) - 16.5 + 4.8 \times \delta^{18}\text{O}_C(V - PDB))}{4.8} \quad (\text{eq. 8})$$

463 The calculated $\delta^{18}\text{O}_{sw}$ reflects a combination of changes in global ice volume and local
464 changes in $\delta^{18}\text{O}_{sw}$ attributable to local salinity changes. We compare overall changes in
465 $\delta^{18}\text{O}_{sw}$ at each site which approximates changes in salinity (Rohling et al., 2007). Calculation
466 of absolute salinity requires assumptions regarding the relationship between $\delta^{18}\text{O}_{sw}$ and
467 salinity at a regional level and how this relationship has changed in the past. Thus, due to the
468 large uncertainties associated with this assumption we interpret the $\delta^{18}\text{O}_{sw}$ record in terms of
469 salinity variations but do not calculate absolute salinity.

470

471 **3. Results**

472 **3.1 Mg/Ca records from the middle Miocene**

473 At ODP Sites 806 and 761, planktic Mg/Ca decreases across the MMCT (14-13 Ma) along
474 with the positive increase in benthic foraminiferal $\delta^{18}\text{O}$ ($\delta^{18}\text{O}_b$) indicative of cooling and
475 Antarctic glaciation (Fig. 2C). A point to point comparison shows that ODP Site 806 *D.*
476 *altispira* Mg/Ca declines by 0.60 mmol/mol (i.e. 3.85 to 3.25 mmol/mol) and 761 *T.*
477 *trilobatus* Mg/Ca declines by 0.90 mmol/mol (i.e. 4.6 to 3.5 mmol/mol) (Fig. 2C) from 14.0

478 to 13.0 Ma. Average Mg/Ca values in the warm MCO (16.5-15 Ma) were higher than post-
479 MMCT (13-11.5 Ma) at both sites (Fig. 2C) with ODP Site 806 Mg/Ca values decreasing
480 from 3.7 to 3.5 mmol/mol and ODP Site 761 Mg/Ca values decreasing from 4.1 to 3.8
481 mmol/mol, respectively. During the MCO, both Mg/Ca records show short-term variations
482 with higher Mg/Ca ratios aligning with more negative $\delta^{18}\text{O}_b$ values or periods of
483 warmth/reduced ice volume. Overall the similarities in planktic Mg/Ca and $\delta^{18}\text{O}_b$ suggest that
484 Mg/Ca is reflecting temperature variations across the middle Miocene.

485

486 **3.2 Sensitivity Analysis**

487 As stated previously, to consider the potential impact of pH and salinity changes on the
488 long-term trends in Mg/Ca, we perform a sensitivity analysis. Specifically, we consider the
489 influence of (1) varying pH and salinity on *D. altispira* Mg/Ca-SST and $\delta^{18}\text{O}_{sw}$ estimates and
490 (2) varying salinity on *T. trilobus* Mg/Ca-SST and $\delta^{18}\text{O}_{sw}$ estimates.

491 As specified in section 2.5, we employ a pH and salinity correction to *D. altispira* Mg/Ca
492 ratios to examine the influence on the long and short-term trends in Mg/Ca (Fig. 3). The
493 magnitude of uncertainty on the Mg/Ca temperatures due to unconstrained salinity variations
494 is $\pm 1^\circ\text{C}$ (Fig. 3A). The pH-corrected and pH-uncorrected *D. altispira* Mg/Ca record shows
495 similar values following the MMCT with a gradual increase in Mg/Ca. However, during the
496 MCO the pH corrected and uncorrected Mg/Ca records diverge with the pH corrected Mg/Ca
497 lower by ~ 0.3 mmol/mol equivalent to $\sim 1^\circ\text{C}$ (Fig. 3B). During the MCO, the pH corrected
498 Mg/Ca record shows lower average Mg/Ca values relative to the post-MMCT time interval.
499 However, both pH corrected and pH uncorrected Mg/Ca records show a cooling associated
500 with the MMCT and similar short-term variations during the MCO (i.e. higher Mg/Ca values
501 during the warm periods) (Fig. 3B).

502

503 As stated in section 2.5, some species, such as symbiont bearing *T. sacculifer* are insensitive to
504 pH changes. In the same vein, it is therefore possible that *D. altispira*, a symbiont bearing
505 species as well, might have a similarly muted response. Additionally, more work is needed to
506 identify the controlling carbonate system parameter on foraminifera, given that some studies
507 suggest pH or DIC. We also acknowledge that without a site specific pH reconstruction, it is
508 difficult to determine if the boron isotope pH derived record from the Indian and Pacific
509 Ocean is representative for the WPWP region. Considering these uncertainties and unknowns,
510 here we employ the multi-species calibration from Anand et al., (2003) (eq. 6) to estimate
511 SSTs in the WPWP. To account for the uncertainty associated with pH and salinity variations,
512 we incorporate an uncertainty envelope of $\pm 2^\circ\text{C}$ from 16.5 to 13.0 Ma and $\pm 1^\circ\text{C}$ from the

513 13.0 to 11.5 Ma in the ODP Site 806 SST reconstruction and present an associated uncertainty
514 enveloped in the corresponding $\delta^{18}\text{O}_{\text{sw}}$ reconstruction.

515

516 As specified section 2.5, to convert *T. trilobus* Mg/Ca into temperature, we apply the Gray
517 and Evans (2019) temperature equation with variable seawater Mg/Ca estimates from this
518 study. Sosdian et al., (2020) use a constant Miocene Mg/Ca_{sw} value of 3.43 mol/mol which is
519 within the range of Miocene Mg/Ca_{sw} values (3.4-3.9 mol/mol) applied here. The
520 recalculated SST record from *T. trilobus* Mg/Ca data presented in Sosdian et al., (2020) has
521 lower absolute values in comparison to the Sosdian et al., (2020) estimates but similar short-
522 term and long-term trends (Figure S8). We consider this a more appropriate approach as the
523 polynomial regression used in this study includes compiled seawater Mg/Ca proxy records
524 from a range of approaches.

525

526 We perform a sensitivity analysis to consider changes in salinity and its influence on the SST
527 record. Figure 4 shows the three SST and $\delta^{18}\text{O}_{\text{sw}}$ reconstructions for the salinity sensitivity
528 analysis. The magnitude of uncertainty on the Mg/Ca temperatures due to unconstrained
529 salinity variations is $\pm 1^\circ\text{C}$. To account for the salinity uncertainty we incorporate an
530 uncertainty envelope of $\pm 1^\circ\text{C}$ in the ODP Site 761 SST reconstruction and present an
531 associated uncertainty enveloped in the $\delta^{18}\text{O}_{\text{sw}}$ reconstruction.

532

533 Here we also revisited the *G. bulloides* Mg/Ca dataset from Shevenell et al., (2004). These
534 authors used the Mashiotta et al., (1999) Mg/Ca-T equation and assumed modern Mg/Ca_{sw} to
535 calculate SST. Here, we calculate SST in the similar manner to the *T. trilobus* record where
536 we apply the Gray and Evans (2019) equation with variable Mg/Ca_{sw} (this study) and pH
537 correction. We perform a salinity sensitivity analysis in the similar vein as above. Figure S9
538 shows the SST reconstructions from the salinity sensitivity analysis. The magnitude of
539 uncertainty on the Mg/Ca temperatures due to unconstrained salinity variations is $\pm 0.5^\circ\text{C}$.

540 As expected, the ODP 1171 recalculated Mg/Ca-SST record has higher absolute values, due
541 to lower Mg/Ca_{sw} values used to estimate SST. The overall short-term and long-term trends
542 are similar to the original record (Shevenell et al., 2004; Figure S9). To account for the
543 salinity uncertainty we incorporate an uncertainty envelope of $\pm 0.5^\circ\text{C}$ in the SST
544 reconstruction.

545

546 In section 3.2 we present and review the main features of ODP Site 806 and revisited ODP

547 site 761 Mg/Ca-SST reconstructions with their corresponding uncertainty envelopes as
548 specified above. Alongside this, we present the $\delta^{18}\text{O}_{\text{sw}}$ reconstructions with an uncertainty
549 envelope as specified above. Overall when comparing the SST and $\delta^{18}\text{O}_{\text{sw}}$ trends, we present
550 the relative anomaly, as relative change with respect to baseline average from 15.5-16.0 Ma,
551 with uncertainty envelopes as specified above. This approach helps avoid additional
552 uncertainties on absolute values associated with the factors mentioned above (e.g. Mg/Ca_{sw},
553 diagenesis).

554

555

556 3.2 Mg/Ca-temperature and $\delta^{18}\text{O}$ history

557 The near-surface dwelling species *D. altispira* Mg/Ca temperature record of ODP
558 Site 806 in the western equatorial Pacific broadly varies by 2°C between cold and warm
559 periods. From 14.1 to 13.7 Ma, SSTs in the western equatorial Pacific sharply cooled by
560 ~1.8°C coincident with Antarctic glaciation and the positive $\delta^{18}\text{O}_b$ excursion at ODP Site 806
561 (Figure 5A). However, following the MMCT the reconstructed SST record shows a gradual
562 long-term warming of ~1°C from 13.5 to 11.5 Ma.

563 The *D. altispira* $\delta^{18}\text{O}_p$ data from this study compare well with the previously
564 published *D. altispira* and *T. trilobus* $\delta^{18}\text{O}_p$ records from Corfield and Cartlidge (2003) and
565 Nathan and Leckie (2009) and here we compile all these datasets (Figure 5B). Average *D.*
566 *altispira* $\delta^{18}\text{O}_p$ decreases from the early MCO (-0.76‰) to the lowest values around ~ 15 Ma
567 (-1.25‰), followed by a small increase following the MMCT (to -0.92‰). The compiled *D.*
568 *altispira* $\delta^{18}\text{O}_p$ long-term trend does not bear resemblance to the Mg/Ca-SST record at this
569 site indicating that the $\delta^{18}\text{O}_p$ signal largely reflects changes in surface ocean $\delta^{18}\text{O}_{\text{sw}}$. The *D.*
570 *altispira* $\delta^{18}\text{O}_p$ record differs markedly from the $\delta^{18}\text{O}_b$ with no change across the climate
571 transition itself, suggesting that variations in local salinity are compensating for the global
572 increase in $\delta^{18}\text{O}_{\text{sw}}$ caused by the glaciation.

573 The surface dwelling *T. trilobus* Mg/Ca-SST record from eastern equatorial Indian
574 Ocean ODP Site 761 shows small long-term 1.5°C cooling across the middle Miocene
575 calculated by averaging the SST estimates from before and after 14.0-13.5 Ma. This small
576 long-term cooling is punctuated by a sharp 2.8°C cooling from 14.0 to 13.8 Ma concomitant
577 with the positive benthic $\delta^{18}\text{O}_b$ excursion from 14.1 to 13.9 Ma indicative of a sea level
578 change associated with Antarctic glaciation (Holbourn et al., 2004; Lear et al., 2010; John et
579 al., 2011) (Fig. 6). SSTs varied by ~3°C between warm, deglaciated and cool, glaciated
580 conditions prior to the MMCT. Around 13.5 Ma following the sharp decrease in temperature
581 and transition into the stable icehouse of today, SSTs varied by 2°C.

582 The middle Miocene long-term cooling and decrease in SST variability are not
583 reflected in the corresponding $\delta^{18}\text{O}_p$ record (Fig. 6). Average $\delta^{18}\text{O}_p$ decreases from the early
584 MCO (-0.45 ‰) to the late middle Miocene (-0.87 ‰). $\delta^{18}\text{O}_p$ values show a sharp positive
585 excursion of 0.86 ‰ synchronous with the SST cooling and $\delta^{18}\text{O}_b$ excursion from 14.1-13.9
586 Ma followed by a return to average pre-excursion values. The $\delta^{18}\text{O}_p$ (Fig. 6B) record shows a
587 long-term decrease at this site indicative of a possible freshening and fluctuates considerably
588 across the middle Miocene implying that substantial variations in salinity are superimposed
589 on the $\delta^{18}\text{O}_p$ curve.

590 Using the Mg/Ca-derived SST records from ODP Sites 806 and 761 we reconstruct
591 variations in $\delta^{18}\text{O}_{sw}$ at both sites (Figure 7B). ODP Site 806 $\delta^{18}\text{O}_{sw}$ shows short-term
592 variability during cold and warm periods prior to the MMCT with no discernible change in
593 $\delta^{18}\text{O}_{sw}$ across the middle Miocene or the MMCT. In agreement with ODP Site 806, ODP Site
594 761 shows similar short term changes across the middle Miocene but of larger magnitude
595 with variations ~ 1 ‰ pre-MMCT, with fresher conditions during cooler, icier intervals and
596 saltier conditions during warmer, less icy intervals. In contrast to the indiscernible long-term
597 change at ODP Site 806, the ODP Site 761 $\delta^{18}\text{O}_{sw}$ record shows a long-term freshening trend
598 from the warmth of the MCO to the post-MMCT conditions. This is punctuated by a sharp
599 freshening from 13.9-13.4 Ma following by small amplitude (~ 0.5 ‰) variability post-
600 MMCT. Overall these $\delta^{18}\text{O}_{sw}$ records indicate a dynamic hydrologic history of the Indo-
601 Pacific region and that the Indian Ocean freshened relative to the Pacific following the major
602 glaciation step at 13.9 Ma. Although we do caveat that due to the low resolution of the ODP
603 806 SST record and its associated uncertainties (pH, salinity correction), interpretation of the
604 806 $\delta^{18}\text{O}_{sw}$ record might evolve with a more detailed evaluation of salinity changes at this site
605 and the Mg/Ca-pH sensitivity for *D. altispira*.

606

607 **4. Discussion**

608 Our new trace metal and stable isotope records span a 5 Myr interval from the warmth of the
609 MCO through the MMCT (Fig. 5-7). Here we examine the overall features of the SST and
610 $\delta^{18}\text{O}_{sw}$ records across the middle Miocene on short and long-term (>1 Myr) time scales in
611 context of global changes in $p\text{CO}_2$ and ice volume to constrain the global nature of these
612 changes and any tropical-high latitude linkages. Further, we examine changes in
613 paleogeography and constriction of the Indonesian Seaway in driving regional surface
614 hydrography changes in the eastern tropical Indian Ocean.

615

616 **4.1. Tropical Sea Surface Cooling across the middle Miocene**

617 Previously, the magnitude and nature of temperature change deduced from low latitude
618 isotopic records across the middle Miocene has been contentious (Stewart et al., 2004).
619 Earlier isotopic studies of the tropical region suggested a warming in the Indo-Pacific region
620 across the middle Miocene in contrast to our findings (Savin et al., 1985). Reconstruction of
621 Miocene atmospheric CO₂ concentrations show higher than modern values of ~470-630 ppm
622 from 17-15 Ma, with large swings in CO₂ concentrations during the MCO and a decline in
623 CO₂ concentration across the MMCT of ~200 ppm (Foster et al., 2012; Badger et al., 2013;
624 Greenop et al., 2014; Sosdian et al., 2018). These dynamic changes in CO₂ concentration
625 occur alongside the waxing and waning of ice sheets and sea level (Figure 7; Lear et al., 2010;
626 John et al., 2011). Under the high CO₂ concentrations of the MCO, climate models simulate a
627 warmer-than-modern tropical Indo-Pacific region (Tong et al., 2009; Krapp & Jungclauss,
628 2011). Here we examine relative changes in Indo-Pacific SSTs, in lieu of examining absolute
629 SSTs relative to modern, due to the uncertainties associated with estimating absolute SSTs in
630 the middle Miocene.

631 During the MCO, the Indo-Pacific cooling and warming is tightly coupled to the
632 waxing and waning of the ephemeral ice sheets and CO₂ (Figure 7). This is evident at 15.5
633 Ma where SSTs were warm during an interval of high pCO₂, high sea level stand, and warm
634 deep ocean waters. At 15 Ma SSTs cool during an interval of low CO₂ concentrations, low sea
635 level, and cool deep ocean waters (Shevenell et al., 2004; Lear et al., 2010; Foster et al., 2012;
636 Sosdian et al., 2018). The orbitally resolved South China Sea SST record exhibits a SST
637 pattern that generally follows this trend during the MCO (Holbourn et al., 2010) suggesting a
638 tropics-wide response. During the MCO, temperature records in both the high and low
639 latitudes are responding in a similar manner, evident from comparison of SST records from
640 ODP Site 1171 and from this study (Fig. 8; Shevenell et al., 2004; Sosdian et al., 2020).
641 Although correlation of age models is difficult due to differences in available stratigraphic
642 datums at each site, from 16.8 to 16.2 Ma both the high latitudes and tropics were warming
643 together, evident when comparing similarly resolved SST records from ODP Sites 761 and
644 1171 (Fig. 8; Figure S10, S11). Overall, these oscillations in the Indo-Pacific region suggest
645 that the tropics responded dynamically to changes in greenhouse gas forcing, alongside
646 Antarctic ice sheet dynamics and high latitude temperature change.

647

648 Following the warmth of the MCO, atmospheric CO₂ concentrations declined with a
649 punctuated CO₂ decrease associated with the glaciation event at 13.9 Ma (Foster et al., 2012;
650 Badger et al., 2013; Sosdian et al., 2018). The 1.8-2.8°C cooling in the low latitude Indo-
651 Pacific region is associated with the glaciation event and CO₂ decline at 13.9 Ma (Holbourn et
652 al. 2004; Lear et al., 2010; Badger et al., 2013; Foster et al., 2012; Sosdian et al., 2018). A

653 low resolution alkenone-derived SST record from the eastern equatorial Pacific shows a 2 °C
654 transient cooling around 14 Ma consistent with our findings and indicating a tropics wide
655 response, although the reconstructed temperatures surrounding this transient cooling event are
656 near the saturation limit of the proxy and the cooling may be a low end estimate (Rousselle et
657 al., 2013). However, an orbitally resolved SST record from ODP Site 1146 in the SCS shows
658 no long-term cooling across the MMCT but rather discrete warming events from 14.6 Ma
659 onward associated with glaciation. These lines of evidence suggest that despite its tropical
660 location the Indo-Pacific was not insensitive to temperature change across the middle
661 Miocene. Further the tropics cooled in the EEP and Indo-Pacific region across the MMCT
662 but distinct differences exist regionally in the tropical surface ocean across the Miocene.

663

664 Across the MMCT, the orbitally resolved Southern Ocean SST record shows three distinct
665 cooling steps at 14.2, 14.0 and 13.9 Ma of a total magnitude of 6-7 °C (Figure 8; Figure S10)
666 (Shevenell et al., 2004). This ODP Site 1171 SST record is of higher resolution (~9 kyr)
667 across the MMCT interval (45 data points; 14.2 to 13.8 Ma) than ODP Site 761 (~37 kyr; 10
668 data points) and ODP Site 806 (~150 kyr; 3 data points) which makes a point to point
669 comparison difficult. However, examination of the temperature trends at each site shows that
670 the Indo-Pacific cooling step initiated at 14.0 Ma occurs synchronous with the final two steps
671 in the Southern Ocean cooling (Figure 8).

672

673 This interpretation of the lead/lag nature of the SST records from the Indo-Pacific and
674 Southern Ocean hinges on how tightly constrained site specific age models are, and whether
675 the lead/lags could be within error of the age model across the middle Miocene. Overall, there
676 are several reasons to support the interpretation of the lead of Southern Ocean cooling over
677 the tropical Indian Ocean. The age model for ODP Site 1171 was developed based on 11
678 magneto- and five biostratigraphic (foraminifer) and seven stable isotope datums (Shevenell
679 & Kennett, 2004) and has not been updated since original publication. The age model for
680 ODP Site 761 is a fourth order polynomial fit based on the biostratigraphic and isotopic
681 datums from Holbourn et al., (2004) and ODP Site 806 age model is based on fourth order
682 polynomial fit through nannofossil and planktic foraminiferal biostratigraphical events (Lear
683 et al., 2015). All biostratigraphic datums are on the on the Berggren et al., (1995) timescale.
684 Within each record there are several datums that anchor the MMCT and further each site has
685 a highly resolved $\delta^{18}\text{O}_b$ and $\delta^{13}\text{C}_b$ records that allow comparison to the individual SST
686 records (Figure S10-S12; Table S1). The three step cooling as exhibited in the ODP Site 1171
687 Mg/Ca-SST record (14.2, 14.0, 13.9 Ma) precedes the positive $\delta^{18}\text{O}_b$ excursion (13.9 Ma),
688 indicative of Antarctic ice growth by 0.30 Myr, whilst the cooling exhibited in the ODP Site

689 761 Mg/Ca-SST record (14.0 Ma) occurs in step with the positive $\delta^{18}\text{O}_b$ excursion (14.0 Ma)
690 (Figure 8). Considering the lower resolution nature of the Mg/Ca-SST relative to the $\delta^{18}\text{O}_b$
691 record, the cooling at ODP Site 806 (13.97 Ma) occurs in step with the positive $\delta^{18}\text{O}_b$
692 excursion (13.91 Ma; Figure 8). In summary, the relative timing of the Mg/Ca-SST cooling
693 compared with the $\delta^{18}\text{O}_b$ and $\delta^{13}\text{C}_b$ shifts are different at each site and suggest that the
694 Southern Ocean cooling leads the Indo-Pacific by a few hundred thousand years (Figure 8).
695

696 The lead of Southern Ocean cooling versus ice volume has been tied to the decoupling of
697 Southern Ocean surface hydrography and global ice volume, caused by circulation changes
698 and/or thresholds for Antarctic ice growth (Shevenell et al., 2004). These new records support
699 the global signature of the MMCT cooling from 14.0 to 13.9 Ma and hint that the early
700 cooling in the Southern Ocean is tied to a regional change in climate and/or non-thermal
701 influences on the ODP Site 1171 planktic Mg/Ca record. This indicates that both the high and
702 low latitudes cooled as ice sheets advanced at 13.9 Ma supporting an important role for the
703 carbon cycle in driving the glaciation (e.g., Foster et al., 2012) and/or representing important
704 positive feedbacks (e.g., Badger et al., 2013).

705

706 Post-MMCT, ODP Site 806 shows a gradual overall warming of 1°C from 13.5 to 11.5 Ma.
707 However in contrast, following the MMCT, ODP Site 761 shows short term minor variations
708 in SST but no long-term trend in SST from 13.5 to 11.5 Ma. SSTs from exceptionally well
709 preserved foraminifera $\delta^{18}\text{O}_p$ records in Tanzania show a warming from 12.2 to 11.55 Ma,
710 however this is based on only two time slices (Stewart et al., 2004). Available organic-based
711 SST records from the middle late Miocene derive mostly from locations outside of the
712 WPWP, due to the saturation of the proxy in SST greater than 29°C . A $\text{U}^{k'}_{37}$ -derived SST
713 record from EEP across the late middle Miocene shows no long-term change in SST
714 (Rouselle et al., 2003) across the late middle Miocene. Other available $\text{U}^{k'}_{37}$ -derived SST
715 record only capture ~ 12.5 to 11.5 Ma and show no discernible long-term change in SSTs
716 (Zhang et al., 2014; Herbert et al., 2016).

717

718 The gradual warming at ODP Site 806 could be driven by changes in CO_2 levels, however
719 there is considerable uncertainty in CO_2 reconstructions during the late middle Miocene, with
720 estimates showing either change or an increase from 13 Ma to 11 Ma (Bolton et al., 2016;
721 Mejia et al., 2017; Sosdian et al., 2018). A paleogeographic modeling study shows that with a
722 more open Indonesian Seaway the warm pool migrates west into the eastern Indian Ocean and
723 closure acts to reduce the flow through the seaway and warm waters pile up on the eastern
724 part of the seaway (von der Heydt & Dijkstra, 2011). Using $\delta^{18}\text{O}_p$ and foraminiferal

725 assemblage records (64 kyr resolution) from ODP Site 806, Nathan and Leckie (2009)
726 showed there was a dynamic, deep thermocline in the western equatorial Pacific from 13.2 to
727 11.6 Ma with a stable warm pool forming after 11.6 Ma. Thus constriction of the Indonesian
728 Seaway associated with eustatic sea level fall (59 ± 6 m; John et al., 2011) across the MMCT
729 could have altered the position of proto-warm pool and contributed to the gradual warming at
730 ODP Site 806 until the formation of a stable warm pool. However, due to the low resolution
731 nature of the ODP Site 806 SST record and uncertainty in the size and latitudinal extent of the
732 late middle Miocene proto-warm pool, additional higher resolution record from the western
733 equatorial Pacific are needed to fully resolve the evolution of the WPWP and its dynamics.

734

735 **4.2 Tropical Indian Ocean surface freshening across the middle Miocene**

736 Middle Miocene Antarctic cryosphere expansion had the potential to affect the
737 tropical hydrological cycle and cause significant salinity changes (Chiang & Bitz, 2005). In
738 this context, Holbourn et al., (2010) argued that records of South China Sea surface ocean
739 hydrography are attributable to northward migration of the ITCZ induced by southern
740 hemisphere glaciation events and subsequent favoring of the relatively warmer northern
741 hemisphere following 14.5 Ma (Holbourn et al., 2010). Due to the low resolution of the
742 $\delta^{18}\text{O}_{\text{sw}}$ from ODP Site 806 and uncertainty in non-thermal effects on Mg/Ca, we focus our
743 discussion on the ODP Site 761 $\delta^{18}\text{O}_{\text{sw}}$. ODP Site 761 sits outside of the present-day ITCZ
744 influence and thus the proposed northward shift of the ITCZ at 13.9 Ma would place the ITCZ
745 even further north and does not explain the freshening at ODP Site 761 across MMCT. Here
746 we consider the role of Antarctic glaciation and paleogeographic changes during the Miocene
747 as a mechanism to explain the freshening in the tropical eastern Indian Ocean. Specifically,
748 we propose that the freshening in the Indo-Pacific region was related to the constriction of the
749 Indonesian Seaway passages, driven by Antarctic glaciation induced sea level fall and
750 ongoing paleogeographic changes. We explore this mechanism further in Section 4.2.1,
751 examining the influence the Indonesian Seaway has on the regional surface ocean
752 hydrography in the Indo-Pacific Ocean.

753

754 **4.2.1 Miocene Constriction of the Indonesian Seaway**

755 The modern Indonesian Seaway, a critical tropical ocean passageway, transports heat
756 and freshwater from the Pacific into the Indian Ocean (Gordon & Fine, 1996). The nature and
757 type of flow through the Indonesian Seaway is dictated by the positions of deep basins and
758 channels connecting the oceans, the dominant source water, and the openness of the seaway.
759 The intensity and nature of these pathways is likely to have been affected by past changes in
760 eustatic sea level on multiple time scales (Kuhnt et al., 2004). For example, during the Last

761 Glacial Maximum sea level was lower than today by ~120 m. Under these conditions, the
762 modern major deep flow through the Makassar Strait would have still persisted while the
763 shallow Timor Passage would have been exposed and flow reduced (Figure 9).

764

765 Plate reconstructions from Hall et al., (2002) show that SE Asia collided with Australia
766 around 25 Ma, restricting the deep water pathway between the Pacific and Indian Oceans. The
767 Makassar strait would have been wider than today and only shallow and intermediate waters
768 of possibly North Pacific origin would flow through, while shallow flow of water of South
769 Pacific origin possibly continued through Sulawesi and New Guinea. Kuhnt et al., (2004)
770 estimate that the Indonesian Seaway was at its narrowest from 10-5 Ma with no evidence for
771 tectonic changes between 17 and 12 Ma. Further, as stated previously, the openness of the
772 Indonesian Seaway is also key in setting the position of the WPWP and intensity of tropical
773 surface ocean circulation (von der Heydt & Dijkstra, 2011).

774

775 We propose that the eustatic sea level drop (59 ± 6 m; John et al., 2011; Figure 7) at the
776 MMCT restricted the already relatively shallow Indonesian Seaway. The seaway constriction
777 would result in a change in the proportion of source waters transported through shallow
778 passages from primarily warmer, saltier South Pacific water to primarily colder, fresher North
779 Pacific water. The switch in source waters would act to cool and freshen the distal outflow
780 regions of the seaway and the Leeuwin Current, as evident in our ODP Site 761 SST and
781 $\delta^{18}\text{O}_{\text{sw}}$ records (Figure 7).

782 In addition to changes in the source waters, constriction of the Indonesian Seaway
783 might affect the intensity of the proto-Leeuwin Current. Presently, ODP Site 761 is under the
784 influence of the Leeuwin current, an anomalous eastern boundary current, transporting
785 tropical waters poleward along the west Australian coast. The Leeuwin current is primarily
786 fed from Indonesian seaway waters and to some extent remote equatorial Indian Ocean
787 waters and the flow is driven by large scale meridional pressure gradient (Wijffels et al.,
788 2002; Domingues et al., 2007)) (Fig.9). Thus, changes in the nature of the seaways that guide
789 the Indonesian waters from the Pacific to Indian Ocean, are of importance to the Leeuwin
790 Current. Indeed, paleoceanographic records on Cenozoic and Quaternary timescales suggest
791 that Leeuwin current intensity and composition was dictated by changes in source water and
792 Indonesian seaway connectivity (McGowran et al., 1997; Wyrwool et al., 2009; Spooner et
793 al., 2011).

794 Paleontological data along the northwestern shelf of Australia suggest the current
795 flowed episodically in the late Oligocene/earliest Miocene, but it is likely that the initiation of
796 the modern-day Leeuwin like current was established in the middle Miocene when the

797 tectonic structure was favorable (Wyrwoll et al., 2009). Here we postulate that the transport
798 capacity of the Indonesian Seaway would have been restricted as the flow in the shallow
799 passageways would have been minimized and the proto-Leeuwin current reduced. Reduced
800 intrusion of Leeuwin current waters into the Indian Ocean could act to freshen and cool this
801 region through increased northward transport of the opposing current, similar to the West
802 Australian Current. Further, a reduction in Leeuwin Current would enhance coastal upwelling
803 and enhance productivity (Veeh et al., 2000). Planktic to benthic carbon isotopic differences
804 at ODP Site 761, an indicator of productivity, show that following the MMCT this region
805 became more productive (Figure S13) in line with a reduction in the Leeuwin Current.
806 Overall, these findings indicate a significant role for the Indonesian Seaway in development
807 of modern surface ocean circulation in the Tropical Indian Oceans and tropical heat and
808 moisture transport in these regions.

809

810 **5. Summary and Conclusions**

811 Here we present middle Miocene climate records derived from Mg/Ca and oxygen
812 isotopes in planktic foraminifera from the eastern equatorial Indian Ocean and western
813 equatorial Pacific Ocean. Our records show dynamic changes in SST across the middle
814 Miocene with warmer SSTs during the Miocene Climatic Optimum and an abrupt cooling
815 associated with the glaciation step at 13.9 Ma. It appears that the high latitudes cooled first,
816 followed by Antarctic glaciation and concomitant cooling at both high and low latitudes. This
817 finding supports a role for the carbon cycle in driving the glaciation and/or representing
818 important positive feedbacks.

819 The Middle Miocene Climate Transition was associated with a significant freshening
820 of the tropical eastern Indian Ocean relative to the western Pacific Ocean. We speculate that
821 the sea level fall associated with the Antarctic ice sheet expansion constricted the Indonesian
822 Seaway acting to modify the surface ocean circulation and hydrography in the Indo-Pacific
823 region. More detailed records documenting the SST patterns in Pacific are needed to further
824 explore the response and development of the modern western equatorial Pacific Ocean
825 climate setting, and formation of the western Pacific Warm Pool. Nevertheless, it seems that
826 the Middle Miocene Climate Transition represented a key phase of the evolution of tropical
827 climate dynamics.

828

829 **6. Acknowledgements**

830 This research used samples and/or data provided by the International Ocean Discovery
831 Program (IODP). Funding for this research was provided by NERC Grant NE/I006427/1 to
832 CHL. We thank D. Lunt and A. Farnsworth for discussions on the climate implications of this
833 study, P. Moffa Sanchez for constructive criticism on an earlier version of this manuscript, P.
834 Pearson for assistance with foraminiferal taxonomy, and Anabel Morte-Rodenas for lab

- 835 assistance. All data presented in this study are given in the Supplementary Tables and
 836 deposited in the Zenodo online data repository DOI:10.5281/zenodo.4155835.
 837
 838
- 839
 840 **7. References**
- 841 Ali, J. R., S. J. Roberts, and S. J. Hall (1994) The closure of the Indo-Pacific Gateway: a new plate
 842 tectonic perspective, in Proceedings of the international workshop on Neogene evolution of Pacific
 843 Ocean gateways, edited by F. Hehuwat, E. Utomo, and A. Dharma, pp. 10–20, Nishimura, Kyoto.
 844
- 845 Anand, P., H. Elderfield, and M. H. Conte (2003), Calibration of Mg/Ca thermometry in planktonic foraminifera
 846 from a sediment trap time series, *Paleoceanography*, 18(2).
- 847 Badger, M.P.S., Lear, C.H., Pancost, R.D., Foster, G.L., Bailey, T.R., Leng, M.J., Abels, H.A., (2013).
 848 CO₂ drawdown following the middle Miocene expansion of the Antarctic Ice Sheet. *Paleoceanography*
 849 28.
- 850 Barker, S., M. Greaves, and H. Elderfield (2003), A study of cleaning procedures used for foraminiferal Mg/Ca
 851 paleothermometry, *Geochemistry Geophysics Geosystems*, 4.
 852
- 853 Bemis, B. E., H. J. Spero, J. Bijma, and D. W. Lea (1998), Reevaluation of the oxygen isotopic composition of
 854 planktonic foraminifera: Experimental results and revised paleotemperature equations, *Paleoceanography*,
 855 13(2), 150-160.
 856
- 857 Berggren, W.A., Kent, D.V., Swisher, C.C., Aubry, M.P., (1995) A revised Cenozoic geochronology and
 858 chronostratigraphy. In: Berggren, W.A., Kent, D.V., Aubry, M.P., Hardenbol, J. (Eds.), Geochronology Time
 859 Scales and Stratigraphic Correlation: Framework for an Historical Geology. *SEPM Special Publication*, v. 54,
 860 pp.129-212.
 861
- 862 Bialik, O. M., M. Frank, C. Betzler, R. Zammit, and N.D. Waldmann (2019) Two-step closure of the
 863 Miocene Indian Ocean gateway to the Mediterranean, *Scientific Reports*, 9, 8842, doi:10.1038/s41598-
 864 019-45308-7
 865
- 866 Bolton, C.T., Hernandez-Sanchez, M.T., Fuertes, M.A., Gonzalez-Lemos, S., Abrevaya, L., Mendez-
 867 Vicente, A., Flores, J.A., Probert, I., Giosan, L., Johnson, J., Stoll, H.M., (2016). Decrease in
 868 coccolithophore calcification and CO₂ since the middle Miocene. *Nat. Commun.* 7, 13.
- 869 Brennan, S.T., Lowenstein, T.K., Cendon, D.I. (2013). The major ion composition of Cenozoic
 870 seawater: the past 36 million years from fluid inclusions in marine halite. *American Journal of Science*
 871 313, 713-775.
- 872 Broecker, W. S., and T.-H. Peng (1982), Tracers in the Sea, Eldigo, Palisades, New York.
- 873 Chaisson, W.P., Leckie, R.M. (1993). High-resolution Neogene planktonic foraminifer biostratigraphy
 874 of Site 806, Ontong Java Plateau (western equatorial Pacific). In: Berger, W.H., Kroenke, L.W., Mayer,
 875 L.A. (Eds.), Proceedings of the Ocean Drilling Program. *Scientific Results*, vol.130. Ocean Drilling
 876 Program, College Station, TX, pp. 137–178.
 877
- 878 Chiang, J., Bitz, C.M., (2005) Influence of high latitude ice cover on the marine ITCZ, *Climate Dynamics*, 25,
 879 p477-496
 880
- 881 Cleroux, C., E. Cortijo, P. Anand, L. Labeyrie, F. Bassinot, N. Caillon, and J.-C. Duplessy (2008), Mg/Ca and
 882 Sr/Ca ratios in planktonic foraminifera: Proxies for upper water column temperature reconstruction,
 883 *Paleoceanography*, 23(3).

- 884 Coggon, R. M., D. A. H. Teagle, C. E. Smith-Duque, J. C. Alt, and M. J. Cooper (2010),
885 Reconstructing past seawater Mg/Ca and Sr/Ca from mid-ocean ridge flank calcium carbonate veins,
886 *Science*, 327, 1114–1117, doi:10.1126/science.1182252.
- 887 Corfield, R. M., and J. E. Cartlidge (1993), Oxygen and carbon isotope stratigraphy of the middle
888 Miocene, Holes 805B and 806B, in *Proc. ODP, Sci. Results*, vol. **130**, edited by W. H. Berger, L.
889 W. Kroenke, and L. A. Mayer, pp 307–322, Ocean Drilling Program, College Station, Tex.,
890 doi:[10.2973/odp.proc.sr.130.026.1993](https://doi.org/10.2973/odp.proc.sr.130.026.1993).
- 891 Dekens, P. S., D. W. Lea, D. K. Pak, and H. J. Spero (2002), Core top calibration of Mg/Ca in tropical
892 foraminifera: Refining paleotemperature estimation, *Geochemistry Geophysics Geosystems*, 3.
893
- 894 Delaney, M. L., A. W. H. Be, and E. A. Boyle (1985), Li, Sr, Mg, and Na in foraminiferal calcite shells
895 from laboratory culture sediment traps, and sediment cores, *Geochim. Cosmochim. Acta*, 49(6), 1327-
896 1341.
- 897 Dickson, J. A. D. (2002), Fossil echinoderms as monitor of the Mg/Ca ratio of Phanerozoic Oceans,
898 *Science*, 298, 1222–1224.
- 899 Domingues, C. M., M. E. Maltrud, S. E. Wijffels, J. A. Church, and M. Tomczak (2007), Simulated Lagrangian
900 pathways between the Leeuwin Current System and the upper-ocean circulation of the southeast Indian Ocean,
901 *Deep-Sea Research Part II-Topical Studies in Oceanography*, 54(8-10), 797-817.
- 902 Dueñas-Bohórquez, A., R. E. Da Rocha, A. Kuroyanagi, L. J. De Nooijer, J. Bijma, and G. J. Reichart
903 (2011), Interindividual variability and ontogenetic effects on Mg and Sr incorporation in the
904 planktonic foraminifer *Globigerinoides sacculifer*, *Geochim. Cosmochim. Acta*, 75(2), 520–532,
905 doi:10.1016/j.gca.2010.10.006.
- 906 Edgar, K.M., Anagnostou, E., Pearson, P.N., Foster, G.L., (2015) Assessing the impact of diagenesis
907 on delta B-11, delta C-13, delta O-18, Sr/Ca and B/Ca values in fossil planktic foraminiferal calcite.
908 *Geochim. Cosmochim. Acta* 166, 189-209.
909
- 910 Elderfield, H. & G. Ganssen (2000) Past temperature and d¹⁸O of surface ocean waters inferred from
911 foraminiferal Mg/Ca ratios, *Nature*, 405, p. 422.
912
- 913 Evans, D., and W. Müller (2012), Deep time foraminifera Mg/Ca paleothermometry: Nonlinear correction for
914 secular change in seawater Mg/Ca, *Paleoceanography*, 27.
915
- 916 Evans, D., B. S. Wade, M. Henehan, J. Erez, and W. Müller (2016), Revisiting carbonate chemistry
917 controls on planktic foraminifera Mg/Ca: implications for sea surface temperature and hydrology shifts
918 over the Paleocene Eocene Thermal Maximum and Eocene Oligocene transition, *Climate of the*
919 *Past*, 12(4), 819-835.
920
- 921 Evans, D., Sagoo, N., Renema, W., Cotton, L. J., Müller, W., Todd, J. A., et al. (2018). Eocene
922 greenhouse climate revealed by coupled clumped isotope-Mg/Ca thermometry. *P. Natl. Acad. Sci.*
923 *115*(6), 1174-1179. Article.
924 <http://doi.org/10.1073/pnas.1714744115>
925
- 926 Fantle, M. S. and DePaolo, D. J. (2006) Sr isotopes and pore fluid chemistry in carbonate
927 sediment of the Ontong Java Plateau: Calcite recrystallization rates and evidence for a
928 rapid rise in seawater Mg over the last 10 million years. *Geochim. Cosmochim. Acta*
929 70, 3883-3904.
930
- 931 Foster, G. L., C. H. Lear, and J. W. B. Rae (2012), The evolution of pCO₂, ice volume and climate during the
932 middle Miocene, *Earth and Planetary Science Letters*, 341, 243-254.
933
- 934 Fraile, I., S. Mulitza, and M. Schulz (2009), Modeling planktonic foraminiferal seasonality: Implications for
935 sea-surface temperature reconstructions, *Marine Micropaleontology*, 72(1-2), 1-9.

936
937 Gallagher, S. J., M. W. Wallace, C. L. Li, B. Kinna, J. T. Bye, K. Akimoto, and M. Torii (2009), Neogene
938 history of the West Pacific Warm Pool, Kuroshio and Leeuwin currents, *Paleoceanography*, 24.
939
940 Gasperi, J. T., and J. P. Kennett (1992), Isotopic evidence for depth stratification and paleoecology of Miocene
941 Planktonic foraminifera-Western equatorial Pacific DSDP site 289, *Pacific Neogene: Environment, Evolution,
942 and Events*, 117-147.
943
944 Gasperi, J. T., and J. P. Kennett (1993), Vertical thermal structure evolution of Miocene surface
945 waters: Western equatorial Pacific DSDP Site 289, *Mar. Micropaleontol.*, 22(3), 235–254,
946 doi:[10.1016/0377-8398\(93\)90046-Z](https://doi.org/10.1016/0377-8398(93)90046-Z).
947
948 Gordon, A. L., and R. A. Fine (1996), Pathways of water between the Pacific and Indian oceans in the
949 Indonesian seas, *Nature*, 379 (6561), 146-149.
950
951 Gothmann A. M., Stolarski J., Adkins J. F., Schoene B., Dennis K. J., Schrag D. P., Mazur M. and Bender M. L.
952 (2015) Fossil corals as an archive of secular variations in seawater chemistry since the Mesozoic. *Geochim.
953 Cosmochim. Acta* 160, 188–208. <https://doi.org/10.1016/j.gca.2015.03.018>.

954 Gourlan, AT, L. M. Meynadier, C. J. Allègre (2008): Tectonically driven changes in the Indian Ocean
955 circulation over the last 25 Ma: Neodymium isotope evidence. *Earth and Planetary Science
956 Letters*, 267(1-2), 353-364,

957 Greenop, R., Foster, G.L., Wilson, P.A., Lear, C.H. (2014) Middle Miocene climate instability
958 associated with high-amplitude CO₂ variability. *Paleoceanography* 29, 845-853.

959 Gray, W. R., and D. Evans (2019), Nonthermal Influences on Mg/Ca in Planktonic Foraminifera: A
960 Review of Culture Studies and Application to the Last Glacial Maximum, *Paleoceanography and
961 Paleoclimatology*, 34(3), 306-315.
962
963 Hall, R., Reconstructing Cenozoic SE Asia, In Tectonic evolution of Southeast Asia, edited by R. Hall
964 and D. Blundell, *Geol. Soc. Spec. Pub.*, 106, 153–184, 1996.
965
966 Hall, R., (2002) Cenozoic geological and plate tectonic evolution of SE Asia and the SW Pacific:
967 computer-based reconstructions, model and animations, *J. Asian Earth Sci.*, 20, 353–43.
968
969 Hamon, N., Sepulchre, P., Lefebvre, V., and Ramstein, G. (2013) The role of eastern Tethys seaway
970 closure in the Middle Miocene Climatic Transition (ca. 14 Ma), *Clim. Past*, 9, 2687–2702,
971 <https://doi.org/10.5194/cp-9-2687-2013>.
972
973 Hartman, J. D., Sangiorgi, F., Salabarnada, A., Peterse, F., Houben, A. J. P., Schouten, S., Brinkhuis,
974 H., Escutia, C., and Bijl, P. K. (2018) Paleoceanography and ice sheet variability offshore Wilkes
975 Land, Antarctica – Part 3: Insights from Oligocene–Miocene TEX₈₆-based sea surface temperature
976 reconstructions, *Clim. Past*, 14, 1275–1297, <https://doi.org/10.5194/cp-14-1275-2018>, 2018.
977
978 Hasiuk, F. J., and K. C. Lohmann (2010), Application of calcite Mg partitioning functions to the
979 reconstruction of paleocean Mg/Ca, *Geochim. Cosmochim. Acta*, 74(23), 6751-6763.
980
981 Herbert, T. D., Lawrence, K. T., Tzanova, A., Peterson, L. C., Caballero-Gill, R., & Kelly, C. S. (2016). Late
982 Miocene global cooling and the rise of modern ecosystems. *Nature Geoscience*.
983 <https://doi.org/10.1038/ngeo2813>
984
985 Higgins, J. and Schrag, D. (2012), Records of Neogene seawater chemistry and diagenesis in deep-sea
986 carbonate sediments and pore fluids. *Earth Planet. Sci. Lett.* 357, 386-396 (2012).
987
988 Holbourn, A., W. Kuhnt, J. A. Simo, and Q. Y. Li (2004), Middle miocene isotope stratigraphy and
989 paleoceanographic evolution of the northwest and southwest Australian margins (Wombat Plateau and Great
990 Australian Bight), *Palaeogeography Palaeoclimatology Palaeoecology*, 208(1-2), 1-22.
991

- 992 Holbourn, A., W. Kuhnt, M. Regenberg, M. Schulz, A. Mix, and N. Andersen (2010), Does Antarctic glaciation
993 force migration of the tropical rain belt?, *Geology*, 38(9), 783-786.
- 994 Holbourn, A., Kuhnt, W., Frank, M., Haley, B.A. (2013), Changes in Pacific Ocean circulation
995 following the Miocene onset of permanent Antarctic ice cover. *Earth and Planetary Science Letters*
996 365, 38-50.
- 997 Holbourn, A.E., Kuhnt, W., Lyle, M.W., Schneider, L., Romero, O., and Andersen, N. (2014), Middle
998 Miocene climate cooling linked to intensification of eastern equatorial Pacific upwelling: *Geology*, v.
999 42, p. 19–22, doi:10.1130/G34890.1.
- 1000
1001 Holland, K., Branson, O., Haynes, L., Honisch, B., Allen, K.A., Russell, A.D. et al. (2020),
1002 Constraining multiple controls on planktic foraminifera Mg/Ca,
1003 *Geochim. Cosmochim. Acta.*, v. 273, 116-136, <https://doi.org/10.1016/j.gca.2020.01.015>.
- 1004 Hollis, C. J., et al. (2019), The DeepMIP contribution to PMIP4: methodologies for selection,
1005 compilation and analysis of latest Paleocene and early Eocene climate proxy data, incorporating
1006 version 0.1 of the DeepMIP database, *Geoscientific Model Development*, 12(7), 3149-3206.
- 1007
1008 Hönisch, B., Allen, K.A., Lea, D.W., Spero, H.J., Eggins, S.M., Arbuszewski, J., deMenocal, P.,
1009 Rosenthal, Y., Russell, A.D., Elderfield, H. (2013). The influence of salinity on Mg/Ca in planktic
1010 foraminifers - Evidence from cultures, core-top sediments and complementary delta O-18.
1011 *Geochim. Cosmochim. Acta*, 121, 196-213
- 1012
1013 Horita, J., H. Zimmermann, and H. D. Holland (2002), Chemical evolution of seawater during the
1014 Phanerozoic: Implications from the record of marine evaporites, *Geochim. Cosmochim. Acta*, 66(21),
1015 3733-3756.
- 1016
1017 John, C. M., G. D. Karner, E. Browning, R. M. Leckie, Z. Mateo, B. Carson, and C. Lowery (2011), Timing and
1018 magnitude of Miocene eustasy derived from the mixed siliciclastic-carbonate stratigraphic record of the
1019 northeastern Australian margin, *Earth and Planetary Science Letters*, 304(3-4), 455-467.
- 1020 Kennett, J.P., and Srinivasan, M.S. (1983) *Neogene Planktonic Foraminifera: A Phylogenetic Atlas*:
1021 Stroudsburg, PA: Hutchinson Ross.
- 1022 Kennett, J. P., G. Keller, and M. S. Srinivasan (1985) Miocene planktonic foraminiferal biogeography and
1023 paleoceanography development of the Indo-Pacific region, *Geological Society of America Memoirs*, 163, 197-
1024 236.
- 1025 Key, R.M., Kozyr, A., Sabine, C.L., Lee, K., Wanninkhof, R., Bullister, J.L., Feely, R.A., Millero, F.J.,
1026 Mordy, C., Peng, T.H. (2004) A global ocean carbon climatology: Results from Global Data Analysis
1027 Project (GLODAP). *Global Biogeochemical Cycles* 18.
- 1028 Kisakurek, B., A. Eisenhauer, F. Bohm, D. Garbe-Schonberg, and J. Erez (2008), Controls on shell
1029 Mg/Ca and Sr/Ca in cultured planktonic foraminiferan, *Globigerinoides ruber* (white), *Earth and*
1030 *Planetary Science Letters*, 273(3-4), 260-269.
- 1031
1032 Krapp, M. and Jungclaus, J. H. (2011) The Middle Miocene climate as modelled in an atmosphere-
1033 ocean-biosphere model, *Climates of the Past*, 7, 1169–1188, <https://doi.org/10.5194/cp-7-1169-2011>.
- 1034
1035 Kuhnert, H., T. Bickert, and H. Paulsen (2009), Southern Ocean frontal system changes precede Antarctic ice
1036 sheet growth during the middle Miocene, *Earth and Planetary Science Letters*, 284(3-4), 630-638.
- 1037
1038 Kuhnt, W., A. Holbourn, R. Hall, M. Zuvela, and R. Kase (2004), Neogene history of the Indonesian
1039 throughflow, *Continent-Ocean Interactions within East Asian Marginal Seas*, 149, 299-320.
- 1040
1041 Lear, C. H., H. Elderfield, and P. A. Wilson (2000), Cenozoic deep-sea temperatures and global ice volumes
1042 from Mg/Ca in benthic foraminiferal calcite, *Science*, 287(5451), 269-272.

- 1043
1044 Lear, C. H., E. M. Mawbey, and Y. Rosenthal (2010), Cenozoic benthic foraminiferal Mg/Ca and Li/Ca records:
1045 Toward unlocking temperatures and saturation states, *Paleoceanography*, 25.
- 1046 Lear, CH., Coxall, HK., Foster, GL., Lunt, D., Mawbey, E. M., Rosenthal, Y., Wilson, P. A. (2015).
1047 Neogene ice volume and ocean temperatures: Insights from infaunal foraminiferal Mg/Ca
1048 paleothermometry. *Paleoceanography*, 30, 1437-1454. <https://doi.org/10.1002/2015PA002833>
- 1049 Levy, R., Harwood, D., Florindo, F., Sangiorgi, F., Tripathi, R., et al. (2016) Antarctic ice sheet
1050 sensitivity to atmospheric CO₂ variations in the early to mid-Miocene, *P. Natl. Acad. Sci. USA*, 113,
1051 3453–3458.
- 1052 Lewis, A. R., D. R. Marchant, A. C. Ashworth, S. R. Hemming, and M. L. Machlus (2007), Major middle
1053 Miocene global climate change: Evidence from East Antarctica and the Transantarctic Mountains, *Geological*
1054 *Society of America Bulletin*, 119(11-12), 1449-1461.
- 1055
1056 Lewis, E., and D. W. R. Wallace (1998), Program developed for CO₂ system
1057 calculations, *ORNL/CDIAC-105*, 21 pp., Carbon Dioxide Inf. Anal. Cent., Oak Ridge Natl. Lab., Oak
1058 Ridge, Tenn.
- 1059
1060 Mashiotta TA, Lea DW, Spero H.J. (1999), Glacial–interglacial changes in Subantarctic sea surface
1061 temperature and δ¹⁸O-water using foraminiferal Mg, *Earth and Planetary Science Letters*, 170(4), 417-
1062 432.
- 1063
1064 Majewski, W. & S. M. Bohaty (2010), Surface-water cooling and salinity decrease during the Middle Miocene
1065 climate transition at Southern Ocean ODP Site 747 (Kerguelen Plateau), *Marine Micropaleontology*, 74(1-2), 1-
1066 14.
- 1067
1068 McGowran, B., Q. Li, J. Cann, D. Padley, D.M.McKirdy, S. Shafik (1997) Biogeographic impact of
1069 the Leeuwin Current in southern Australia since the late middle Eocene, *Palaeogeogr. Palaeoclimatol.*
1070 *Palaeoecol.*, 136, pp. 19-40
- 1071
1072 Mejía, L.M., Mendez-Vicente, A., Abrevaya, L., Lawrence, K. T., Ladlow, C., Bolton, C. T., Cacho, I.,
1073 Stoll, H.M. (2017): A diatom record of CO₂ decline since the late Miocene. *Earth and Planetary*
1074 *Science Letters*, 479, 18-33,
- 1075
1076 Nathan, S. A., and R. M. Leckie (2009), Early history of the Western Pacific Warm Pool during the middle to
1077 late Miocene (similar to 13.2-5.8 Ma): Role of sea-level change and implications for equatorial circulation,
1078 *Palaeogeogr. Palaeoclimatol. Palaeoecol.*, 274(3-4), 140-159.
- 1079
1080 Norris, R. D., R. M. Corfield, and J. E. Cartlidge (1993), Evoluton of depth ecology in the planktic foraminifera
1081 lineage Globorotalia (Fohsella), *Geology*, 21(11), 975-978.
- 1082
1083 Pattiaratchi, C. & M. Woo (2009) The mean state of the Leeuwin current system between North West
1084 Cape and Cape Leeuwin, *Journal of the Royal Society of Western Australia*, 92 (2), 221-241
- 1085
1086 Pearson, P.N. (1995). Planktonic foraminifer biostratigraphy and the development of pelagic caps on
1087 guyots in the Marshall Islands group. In: Haggerty, J.A., Premoli Silva, I., Rack, F., McNutt, M.K.
1088 (Eds.), Proc.
- 1089
1090 Pearson, P. N., Ditchfield, P.W., Singano, J., Harcourt-Brown, K., Nicholas, C.J. et al. (2001) Warm
1091 tropical sea surface temperatures in the Late Cretaceous and Eocene epochs. *Nature* 413(6855), pp.
1092 481-487.
- 1093
1094 Rausch, S., Böhm, F., Bach, W., Klügel, A. & Eisenhauer, A. (2013) Calcium carbonate
1095 veins in ocean crust record a threefold increase of seawater Mg/Ca in the past 30
1096 million years. *Earth and Planetary Science Letters*. 362, 215-224.
- 1097
1098 Regenberg, M., D. Nuernberg, S. Steph, J. Groeneveld, D. Garbe-Schoenberg, R. Tiedemann, and W.-C. Dullo

- 1099 (2006), Assessing the effect of dissolution on planktonic foraminiferal Mg/Ca ratios: Evidence from Caribbean
1100 core tops, *Geochemistry Geophysics Geosystems*, 7.
1101
- 1102 Regenberg, M., S. Steph, D. Nuernberg, R. Tiedemann, and D. Garbe-Schoenberg (2009), Calibrating Mg/Ca
1103 ratios of multiple planktonic foraminiferal species with delta O-18-calcification temperatures:
1104 Paleothermometry for the upper water column, *Earth and Planetary Science Letters*, 278(3-4), 324-336.
1105
- 1106 Rohling, E. J. (2007), Progress in paleosalinity: Overview and presentation of a new approach,
1107 *Paleoceanography*, 22(3).
1108
- 1109 Rosenthal, Y., and G. P. Lohmann (2002), Accurate estimation of sea surface temperatures using dissolution-
1110 corrected calibrations for Mg/Ca paleothermometry, *Paleoceanography*, 17(3).
1111
- 1112 Rousselle, G., C. Beltran, M.-A. Sicre, I. Raffi, and M. De Rafelis (2013), Changes in sea-surface conditions in
1113 the Equatorial Pacific during the middle Miocene-Pliocene as inferred from coccolith geochemistry, *Earth and*
1114 *Planetary Science Letters*, 361, 412-421.
- 1115 Sangiorgi, F., Bijl, P. K., Passchier, S., Salzmann, U., Schouten, S., McKay, R., Cody, R. D., Pross, J.,
1116 van de Fliedert, T., Bohaty, S. M., Levy, R., Williams, T., Escutia, C., and Brinkhuis, H. (2018)
1117 Southern Ocean warming and Wilkes Land ice sheet retreat during the mid-Miocene, *Nat. Commun.*, 9,
1118 317, <https://doi.org/10.1038/s41467-017-02609-7>.
- 1119 Savin, S. M., L. Abel, E. Barrera, D. Hodell, J. P. Kennett, M. Murphy, G. Keller, J. Killingley, and E. Vincent
1120 (1985), The evolution of the Miocene surface and near-surface marine temperatures- oxygen isotopic evidence,
1121 *Geological Society of America Memoirs*, 163, 49-&
1122
- 1123 Schlitzer, R. (2012) Ocean Data View. <http://odv.awi.de>.
1124
- 1125 Schneider, N. (1998) The Indonesian Throughflow and the global climate system, *J. Climate*, 11, 676-
1126 689.
1127
- 1128 Sclater, J. G., L. Meinke, A. Bennett, and C. Murphy (1985), The depth of the ocean through the Neogene,
1129 *Geological Society of America Memoirs*, 163, <https://doi.org/10.1130/MEM163-p1>.
1130
- 1131 Scotese, C. R., L. M. Gahagan, and R. L. Larson (1988), Plate tectonic reconstructions of the Cretaceous and
1132 Cenozoic ocean basins, *Tectonophysics*, 155(1-4), 27-48.
1133
- 1134 Sexton, P. F., P. A. Wilson, and P. N. Pearson (2006), Microstructural and geochemical perspectives on planktic
1135 foraminiferal preservation: "Glassy" versus "Frosty", *Geochemistry Geophysics Geosystems*, 7.
1136
- 1137 Shevenell, A. E., J. P. Kennett, and D. W. Lea (2004), Middle Miocene Southern Ocean cooling and Antarctic
1138 cryosphere expansion, *Science*, 305(5691), 1766-1770.
1139
- 1140 Shevenell, A.E., J. P. Kennett (2004), Paleooceanographic Change During the Middle Miocene Climate
1141 Revolution: An Antarctic Stable Isotope Perspective in The Cenozoic Southern Ocean: Tectonics,
1142 sedimentation, and climate change between Australia and Antarctica, N. F. Exon, J. P. Kennett, M. J. Malone,
1143 Eds. (American Geophysical Union, Washington D.C.)
1144
- 1145 Spooner, M. I., P. De Deckker, T. T. Barrows, and L. K. Fifield (2011), The behaviour of the Leeuwin Current
1146 offshore NW Australia during the last five glacial-interglacial cycles, *Global and Planetary Change*, 75(3-4),
1147 119-132.
1148
- 1149 Sprintall, J., Potemra, J. T., Hautala, S. L., Bray, N. A., and W. W. Pandoe (2003) Temperature and
1150 salinity variability in the exit passages of the Indonesian Throughflow. *Deep Sea Res. II*, 50, 2183-
1151 2204.
1152
- 1153 Sosdian, S. M., Greenop, R., Hain, M.P., Foster, G.L., Pearson, P.N., Lear, C.H. (2018) Constraining the
1154 evolution of Neogene ocean carbonate chemistry using the boron isotope pH proxy. *Earth and Planetary*
1155 *Science Letters* 498, 362-376, doi:10.1016/j.epsl.2018.06.017.

- 1156
1157 Sostdian, S.M., T. L. Babila, R. Greenop, G.L. Foster, and C.H. Lear (2020) Ocean carbon storage
1158 across the middle Miocene: a new interpretation for the Monterey Event, *Nat. Commun.* **11**, 134,
1159 <https://doi.org/10.1038/s41467-019-13792-0>
- 1160 Spezzaferri, S., Kucera, M., Pearson, P.N., Wade, B.S., Rappo, S., Poole, C.R., Morard, R., Stalder, C.
1161 (2015) Fossil and Genetic Evidence for the Polyphyletic Nature of the Planktonic Foraminifera
1162 "Globigerinoides", and Description of the New Genus Trilobatus. *Plos One* 10.
- 1163 Stewart, D.R.M., Pearson, P.N., Ditchfield, P.W., Singano, J.W. (2004), Miocene tropical Indian Ocean
1164 temperatures: evidence from three exceptionally preserved foraminiferal assemblages from Tanzania, *Journal of*
1165 *African Earth Sciences*, 40, p. 173-190.
- 1166 Super, J. R., Thomas, E., Pagani, M., Huber, M., O'Brien, C., and Hull, P. M. (2018) North Atlantic
1167 temperature and pCO₂ coupling in the early-middle Miocene, *Geology*, 46, 519–522.
- 1168 Tong, J.A., You, Y., R.D. Müller, Seton, M. (2009) Climate model sensitivity to atmospheric CO₂
1169 concentrations for the middle Miocene, *Global Planetary Change*, 67, p 129-140.
- 1170 Tripathi, A. K., Roberts, C. D., and Eagle, R. A. (2009) Coupling of CO₂ and ice sheet stability over
1171 major climate transitions of the last 20 million years, *Science*, 326, 1394–1397.
- 1172 Veeh, H.H., McCorkle, D.C., Heggie, D.T. (2000) Glacial/interglacial variations of sedimentation on
1173 the West Australian continent margin: constraints from excess
1174 230Th. *Marine Geology*. 166, 11–30.
- 1175
1176 Verducci, M., Foresi, L.M., Scott, G.H., Tiepolo, M., Sprovieri, M., and Lirer, F. (2007) East Antarctic
1177 Ice Sheet fluctuations during the Middle Miocene Climatic Transition inferred from faunal and
1178 biogeochemical data on planktonic foraminifera (Kerguelen Plateau). *U.S. Geological Survey and The*
1179 *National Academics*; USGS OF-2007-1047, Short Research Paper 037.
- 1180
1181 von der Heydt, A.S. & H.A. Dijkstra (2011) The impact of ocean gateways on ENSO variability in the
1182 Miocene. In :Hall, R; Cottam, M.A.; M.E.J. Wilson (eds.). *The SE Asian Gateway: History of*
1183 *tectonics of the Australia-Asia Collision. Geol. Soc. Spec. Pub.*, 355, 305-318.
- 1184
1185 Wajsowicz, R. C., and E. K. Schneider (2001) The Indonesian throughflow's effect on global climate
1186 determined from the COLA coupled climate system, *J. Climate*, 14, 3029–3042, 2001.
- 1187
1188 Wara et al. (2005) Permanent El Nino like conditions during the Pliocene warm period, *Sciece*, v. 309, p. 758-
1189 761.
- 1190
1191 Wijffels, S., J. Sprintall, M. Fieux, and N. Bray (2002), The JADE and WOCE I10/IR6 throughflow sections in
1192 the southeast Indian Ocean. Part 1: water mass distribution and variability, *Deep-Sea Research Part II-Topical*
1193 *Studies in Oceanography*, 49(7-8), 1341-1362.
- 1194
1195 Wyrwool, K.-H., Greenstein, B.J., Kendrick, G.W., Chen, G.S. (2009) The palaeoceanography
1196 of the Leeuwin Current: implications for a future world. *Journal of the Royal Society of Western*
1197 *Australia*, 92, 37-51.
- 1198
1199 Zachariasse, W-J (1992) Neogene planktonic foraminifers from sites 761 and 762 off *Northwest*
1200 *Australia*. In: von Rad, U; Haq, BU; et al. (eds.), *Proceedings of the Ocean Drilling Program, Scientific*
Results, College Station, TX (Ocean Drilling Program), **122**, 665-67.
- 1201
1202 Zhang, Y. G., Pagani, M., & Liu, Z. (2014) A 12-Million-Year Temperature History of the Tropical
1203 Pacific Ocean. *Science*, 344(6179), 84-87. <https://doi.org/10.1126/science.1246172>
1204

1205
1206
1207
1208
1209
1210
1211
1212
1213
1214
1215
1216
1217
1218
1219
1220
1221
1222
1223
1224
1225
1226
1227
1228
1229
1230
1231
1232
1233
1234
1235
1236
1237
1238
1239
1240
1241
1242
1243
1244
1245
1246
1247
1248
1249
1250
1251
1252
1253
1254
1255
1256
1257

Figure Captions

Figure 1 Mean annual sea surface temperature (WOCE; Gouretski & Koltermann, 2004) showing modern locations of ODP sites used in this study (white triangles) and the location of the West Pacific Warm Pool (WPWP) and Indonesian Throughflow. The WPWP is the large body of water in the western Pacific denoted by SSTs greater than 28°C. Sea surface temperature plot made using Ocean Data View (Schlitzer, 2012).

Figure 2 Input parameters for Mg/Ca-temperature sensitivity analysis. (A) interpolated pH estimates derived from the ‘ $\delta^{11}\text{B}_{\text{sw}}\text{-G17}$ ’ reconstruction, fluid inclusion data for $[\text{Mg}^{2+}]$ and $[\text{Ca}^{2+}]$ seawater, and ‘Pälike’ CCD scenario (Sosdian et al., 2018); (B) Fourth order polynomial curve fit through compiled seawater Mg/Ca proxy records based on fluid inclusions, calcite veins, echinoderms, and large benthic foraminifera (Dickson, 2002, Horita et al., 2002, Brennan et al., 2013; Coggon et al., 2010; Rausch et al., 2013; Evans et al. 2018). The grey envelope represents the ± 0.5 mol/mol uncertainty window. (C) Measured Mg/Ca ratios (mmol mol^{-1}) for *D. altispira* and *T. trilobus* from ODP Sites 806 and 761, respectively. Three scenarios for past changes in salinity at ODP Sites 806 and site 761 are explored, specifically assuming modern values for each site and ± 1 PSU modern values.

Figure 3 ODP site 806 Mg/Ca sensitivity analysis output for a range of scenarios. ODP site 806 *D. altispira* Mg/Ca measured in comparison to Mg/Ca corrected for (A) salinity and (B) pH variations.

Figure 4 ODP site 761 Mg/Ca sensitivity analysis output for a range of scenarios. (A) SST estimates derived from ODP site 761 *T. trilobus* Mg/Ca with varying salinity scenarios (constant modern, constant modern +1 PSU, constant modern -1 PSU); (B) $\delta^{18}\text{O}_{\text{sw}}$ records using three salinity scenarios.

Figure 5 Climate proxy data from Ontong Java Plateau ODP Site 806 (0°19.1’N, 159°21.7’E). (A) Mg/Ca-SST anomaly from measured Mg/Ca (black circles) with uncertainty envelope specified in text; (B) planktic foraminifera oxygen isotope records from this study and previously published records (Corfield & Cartlidge, 1993; Nathan & Leckie, 2009); (C) Benthic foraminifera oxygen isotope records from previously published records (Corfield & Cartlidge, 1993; Nathan & Leckie, 2009; Holbourn et al., 2013; Lear et al., 2015). MCO denotes the Miocene Climatic Optimum and MMCT denotes the middle Miocene Climate Transition and the timing is determined from the $\delta^{18}\text{O}_b$ record. Temperature anomaly was calculated as relative temperature change with respect to baseline average from 15.5-16.0 Ma.

Figure 6 Climate proxy data from Wombat Plateau ODP Site 761 (16°44.23’S, 115°32.10’E). (A) Mg/Ca-SST anomaly, generated on planktic foraminifera *T. trilobus* across the middle Miocene (Sosdian et al., 2020) with uncertainty envelope as specified in the text; (B) *T. trilobus* oxygen isotope record from this study; (C) Benthic oxygen isotope records from previously published records (Holbourn et al., 2004; Lear et al., 2010). MCO denotes the Miocene Climatic Optimum and MMCT denotes the middle Miocene Climate Transition and the timing is determined from the $\delta^{18}\text{O}_b$ record. Temperature anomaly was calculated as relative temperature change with respect to baseline average from 15.5-16.0 Ma.

1258 **Figure 7** Site comparison between ODP 806 and 761 (A) Temperature anomaly, as
1259 relative temperature change with respect to baseline average from 15.5-16.0 Ma, determined
1260 from planktic foraminifera Mg/Ca records from this study and Sosdian et al., (2020) with
1261 uncertainty envelope highlighted; (B) planktic $\delta^{18}\text{O}_p$ from *T. trilobus* (blue) and *D. altispira*
1262 (grey) from this study and previously published study (Corfield & Cartlidge, 1993);(C) $\delta^{18}\text{O}_{sw}$
1263 anomaly, as relative $\delta^{18}\text{O}_{sw}$ change with respect to baseline average from 15.5-16.0 Ma and
1264 uncertainty envelope highlighted; (D) Boron isotope derived atmospheric $p\text{CO}_2$ record using
1265 three $\delta^{11}\text{B}_{sw}$ scenarios which incorporate various $\delta^{11}\text{B}_{sw}$ scenarios (LO2; RH13; G17), fluid
1266 inclusion Mg/Casw data, and ‘Palike’ CCD reconstructions (Sosdian et al., 2018). (E)
1267 Eustatic sea level change from the Marion Plateau (John et al., 2011) (F) Estimates of changes
1268 in global ice volume as derived from $\delta^{18}\text{O}_{sw}$ at ODP site 761. The shaded regions showcase
1269 the range in estimates between grey circles are uncorrected BWT estimates whereas dark grey
1270 circles are corrected for changes in deep ocean carbon saturation state changes (Lear et al.,
1271 2010). Note BWT estimates are corrected for changes in Mg/Ca_{sw} . MCO and MMCT denote
1272 the time intervals of the Miocene Climatic Optimum and the middle Miocene Climate
1273 Transition and the timing is determined from the $\delta^{18}\text{O}_b$ record. The 13.9 Ma glaciation step is
1274 highlighted by a purple vertical line. Uncertainty envelopes are included for ODP site 806
1275 records and a uncertainty bar is used for ODP site 761 in panels A and C.
1276

1277 **Figure 8** Comparison of Indo-Pacific ODP Sites 806 and 761 and Southern Ocean site
1278 1171(A, B) Mg/Ca-derived SST anomaly for ODP site 806 and 761 (Sosdian et al., 2020; this
1279 study) and (C) Mg/Ca-derived SST anomaly from ODP site 1171 (Shevenell et al., 2004)
1280 recalculated in this study using the Gray and Evans (2019) multi-variable regression as
1281 specified in the text and variable Mg/Ca_{sw} . Uncertainty envelopes are plotted for each
1282 temperature reconstruction. (D, E) ODP Site 806 and 761 and (F) ODP Site 1171 benthic
1283 oxygen isotope records (Corfield & Cortlidge, 1993; Holbourn et al., 2004; Shevenell et al.,
1284 2004; Nathan & Leckie, 2009; Lear et al., 2010; Holbourn et al., 2013) from across the
1285 middle Miocene (13-15.5 Ma). The blue arrows highlights the cooling steps observed at each
1286 site. The temperature scale is different in panel A-B and C to showcase the variations in each
1287 location. The 13.9 Ma glaciation step is highlighted by a grey vertical line.
1288

1289 **Figure 9** Modern regional surface ocean currents and study sites in the Indo-Pacific region.
1290 Indonesian throughflow straits include Makassar Strait, Lombok Strait, and Timor Passage.
1291 Surface ocean currents include North Equatorial Current (NEC), South Equatorial Current
1292 (SEC), North Equatorial Counter Current (NECC), Leeuwin Current (LC) and Western
1293 Australian Current (WAC). NP (North Pacific) and SP (South Pacific) sources waters are
1294 identified alongside of West Pacific Warm Pool (WPWP). Map made using Ocean Data
1295 View.

1
2
3
4
5
6
7
8
9
10
11
12
13
14
15
16
17
18
19
20
21
22
23
24
25
26
27
28
29
30
31
32

Paleoceanography & Paleoclimatology

Supporting Information for

Initiation of the Western Pacific Warm Pool at the Middle Miocene Climate Transition?

S.M. Sosdian & C.L. Lear

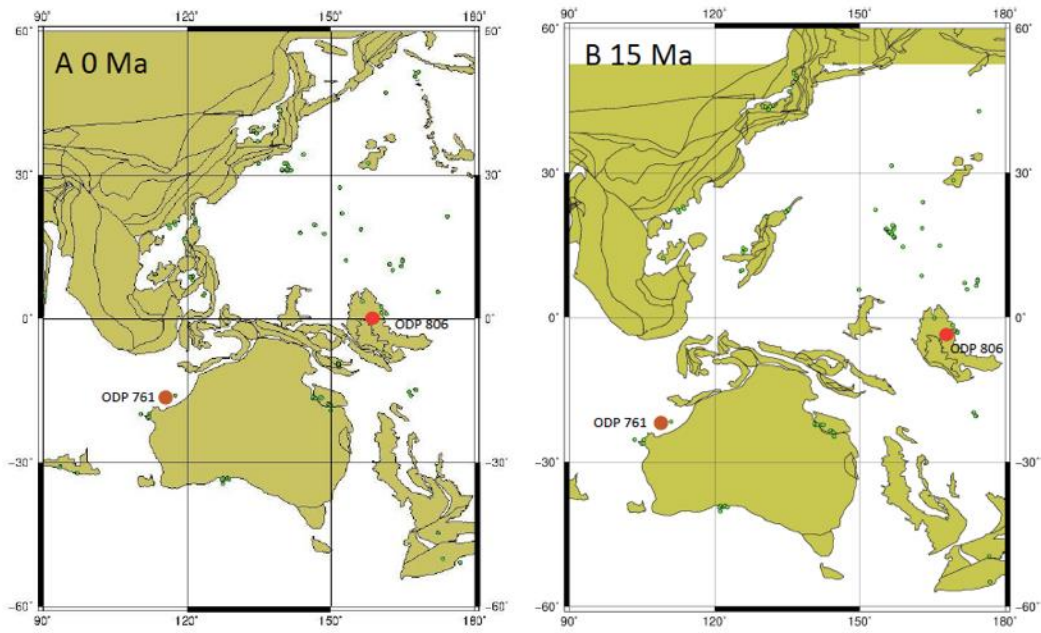
¹Cardiff University, School of Earth & Ocean Sciences, Cardiff, CF10 3AT, UK

Contents of this file

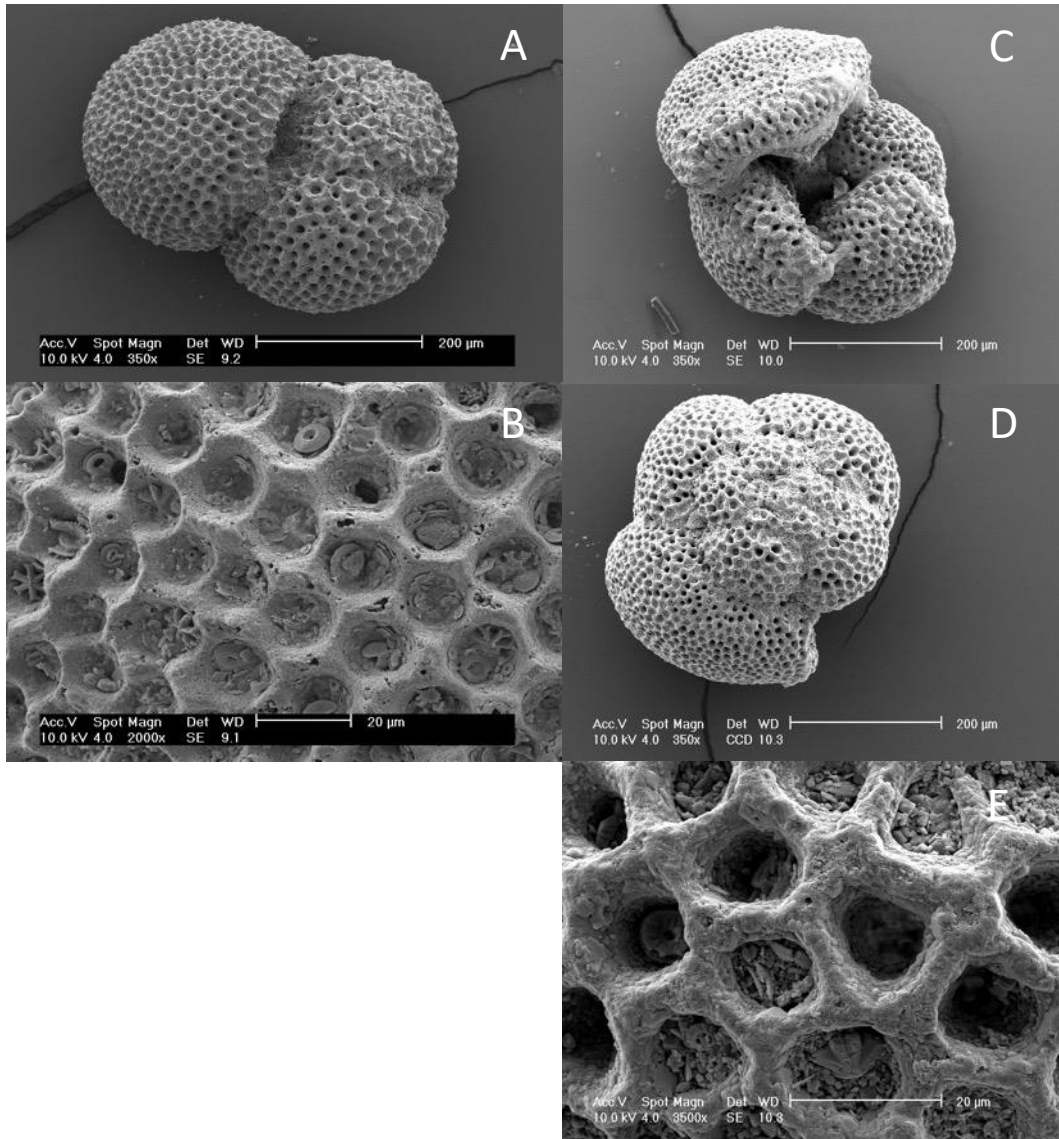
Figures S1 to S13
Tables S1 to S3

Introduction

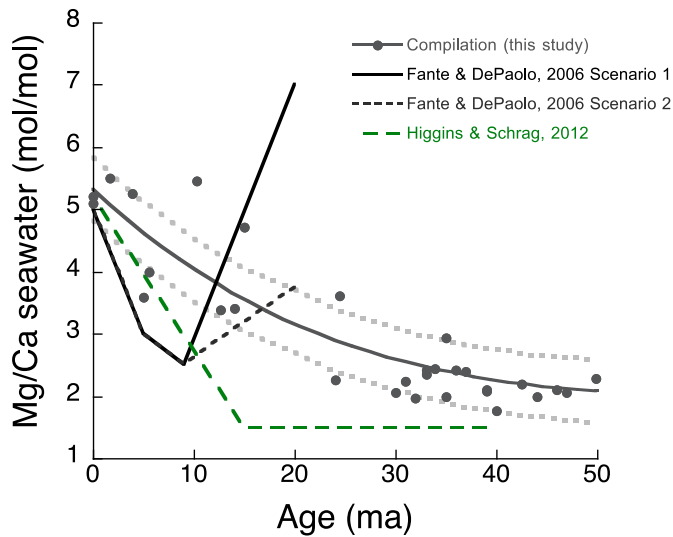
We provide supporting information for our paleoclimate reconstructions associated with site-specific age models, study site locations, sample preservation, and SST sensitivity analysis. Specifically, we provide a map of mid-Miocene paleolocations for sites used in SST reconstructions. We present SEM images from the planktic foraminifera used in the trace metal and isotope records produced in this study and compare records of coarse fraction and average shell size from ODP site 806 and 761 alongside trace metal and isotope records to assess downcore diagenetic alterations. We consider a range of scenarios for recalculating SST from published Mg/Ca datasets and consider site-specific age models associated with each. We provide modern snapshot of the surface ocean salinity alongside locations of key study sites to consider past changes in salinity across the middle Miocene. We compare gradients in planktic and benthic carbon isotopes to explore changes in productivity at ODP site 761. All data are presented in the Supplementary Tables.



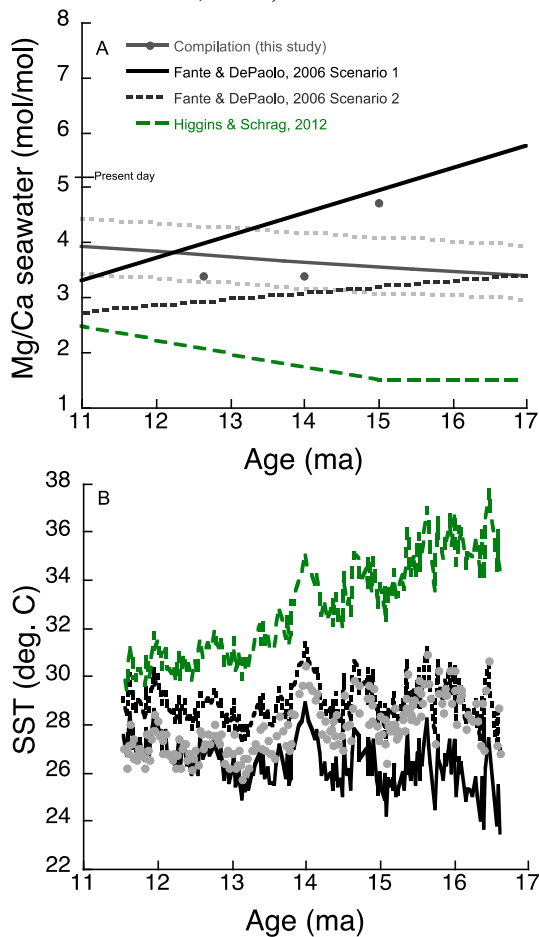
33
 34 **Figure S1** Locations of sites discussed in this study. Paleo-latitude and geographic
 35 reconstruction for (A) 0 and (B) 15.0 Ma were generated from <http://www.odsn.de/>
 36 Green circles represent ODP sites with site 806 and 761 highlighted in red and brown circles,
 37 respectively. Note the long-term northward migration of both ODP sites 806 and 761.



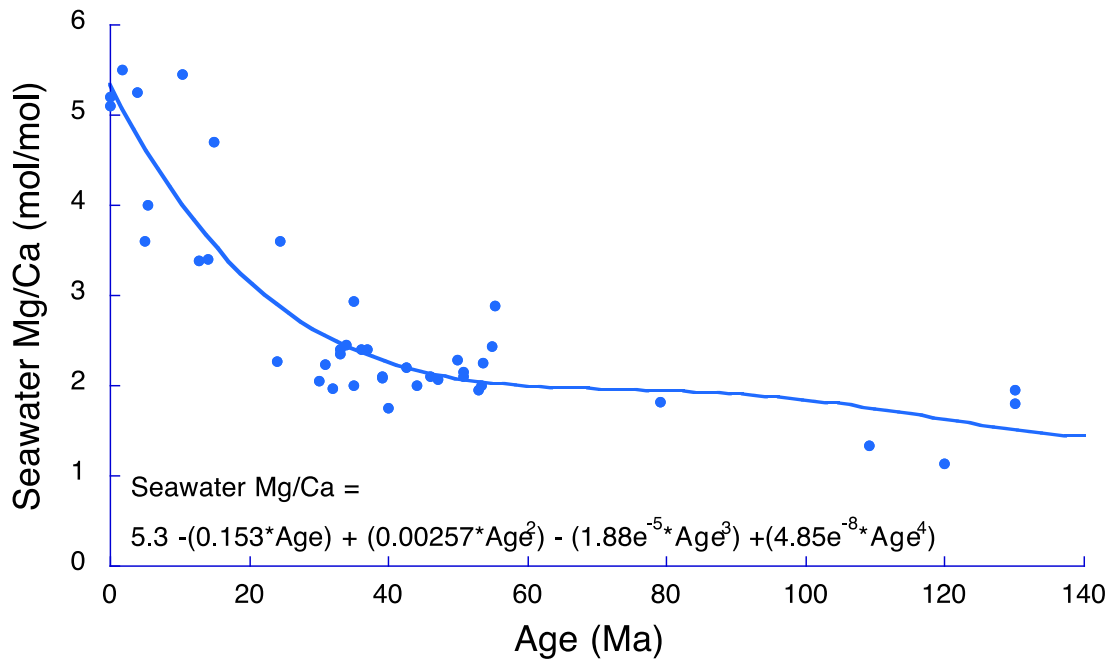
38
 39 **Figure S2** SEM images of species used in this study. (A) Whole test of *T. trilobus* from ODP
 40 761B 05-05 103-105 cm 300-355 μm size fraction (39.73 m below seafloor); (B) Wall
 41 structure of *T. trilobus* test showing original microstructure; (C-D) Whole test spiral and
 42 umbilical side view of *D. altispira*; (E) Wall structure of *D. altispira* test.
 43
 44



45
 46 **Figure S3** Various Mg/Ca seawater reconstructions from a compilation of published proxy
 47 data (this study) and porewater modeling (Fante & DePaolo, 2006; Higgins & Schrag, 2012).
 48 Note a linear fit was used in lieu of the model output for FD06 and HS12 to look at long-term
 49 trends and impact on Mg/Ca-SST trends and consider two scenarios for FD06 as presented in
 50 Fante & DePaola, 2006).

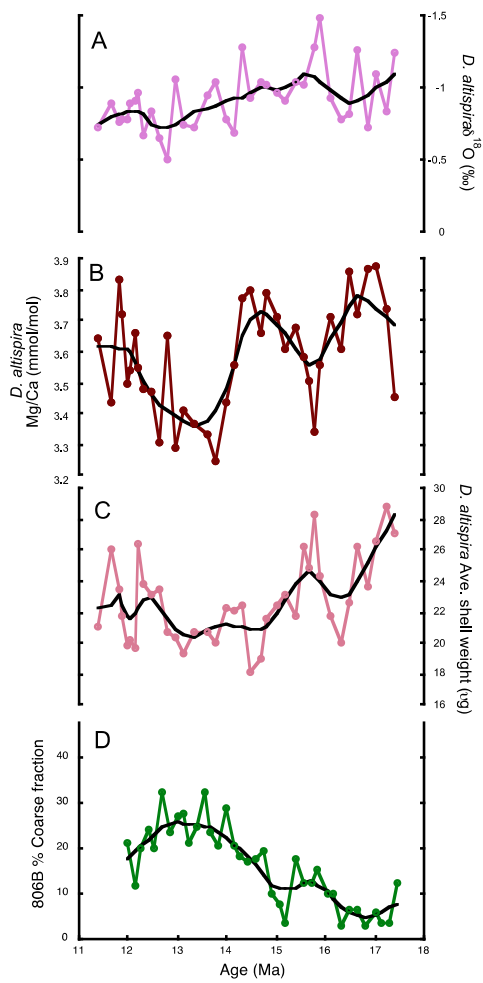


51
 52 **Figure S4** (A) Various Miocene Mg/Ca seawater estimates and (B) corresponding estimated
 53 *T. trilobus* Mg/Ca-SST using the Gray and Evans (2019) equation as specified in the
 54 manuscript.
 55

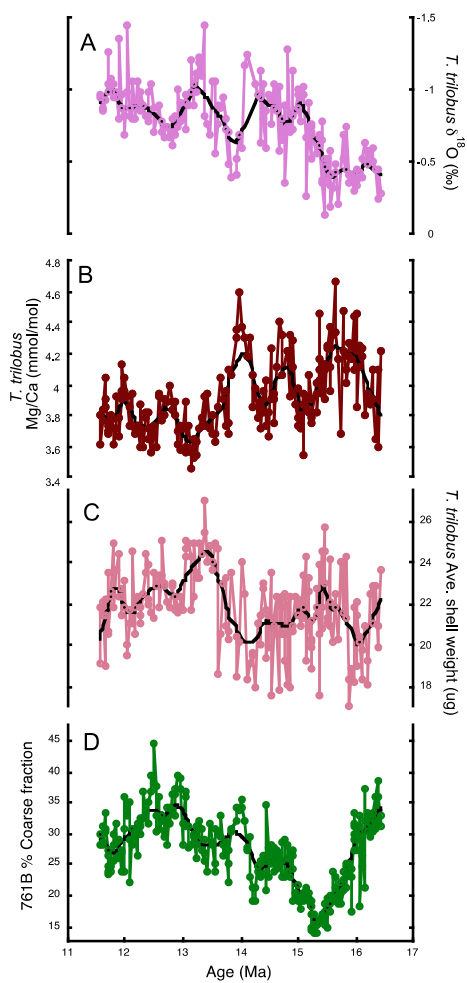


56
 57
 58
 59
 60
 61

Figure S5 Fourth order polynomial curve fit through compiled seawater Mg/Ca proxy records based on fluid inclusions, calcite veins, echinoderms, and large benthic foraminifera (Dickson, 2002, Horita et al., 2002, Brennan et al., 2013; Coggon et al., 2010; Rausch et al., 2013; Evans et al., 2018).

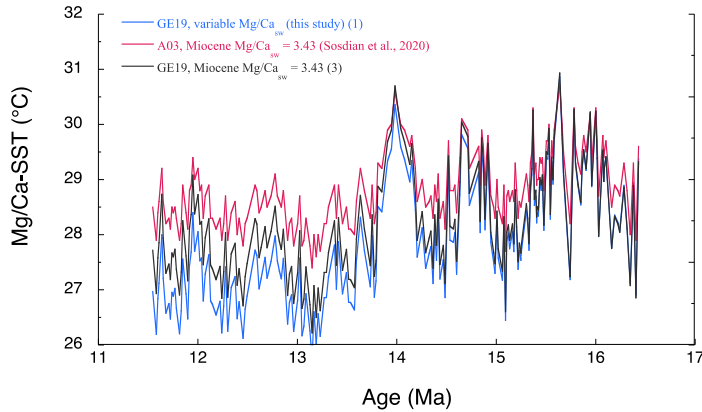


62
 63 **Figure S6** ODP site 806 *D. altispira* $\delta^{18}\text{O}_p$ (A) and Mg/Ca (B) records plotted against (C)
 64 average shell weight and (D) percent coarse fraction. Solid black lines represent 25%
 65 weighted fit line.
 66
 67
 68

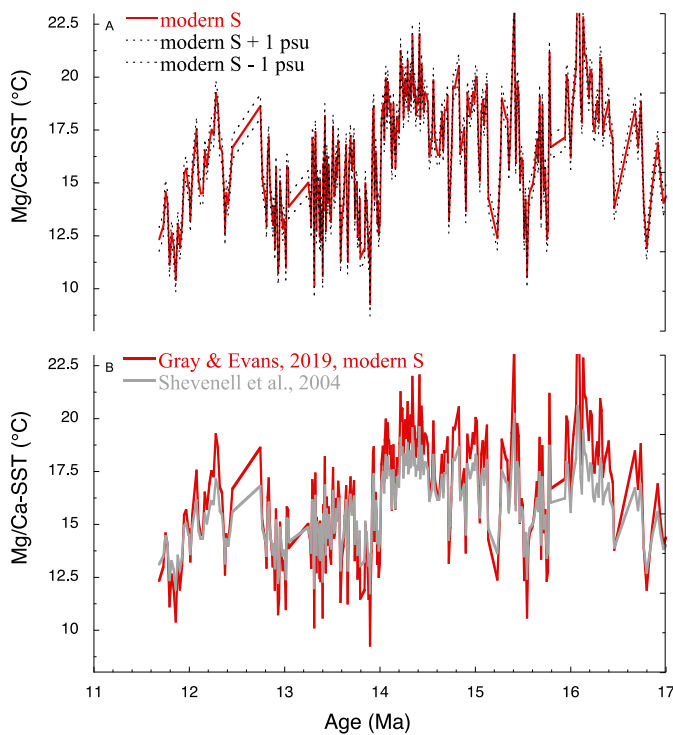


69
 70 **Figure S7** ODP Site 761 (A) *T. trilobus* $\delta^{18}\text{O}_p$ and (B) Mg/Ca ratios (Sosdian et al., 2020)
 71 records plotted alongside (C) average shell weight and (D) coarse fraction. Solid black lines
 72 represent 10% weighted fit line.

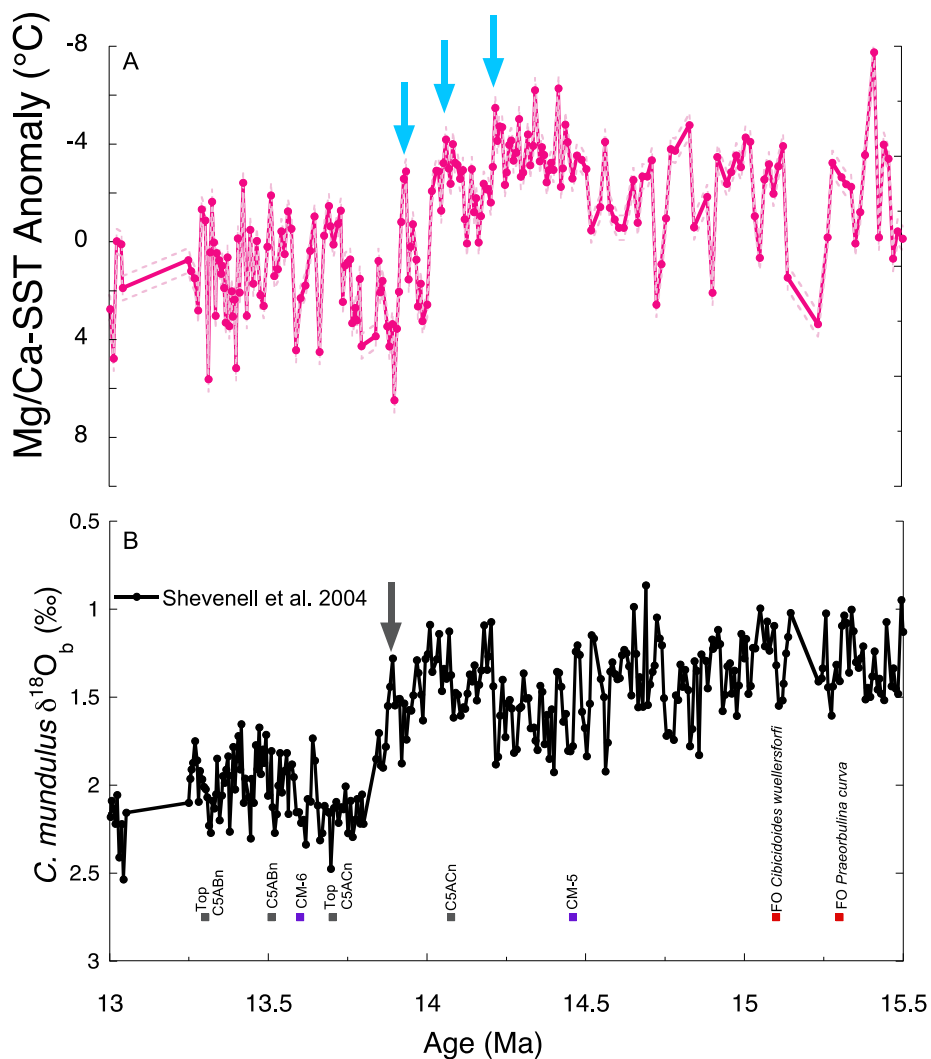
73
 74
 75
 76
 77
 78
 79



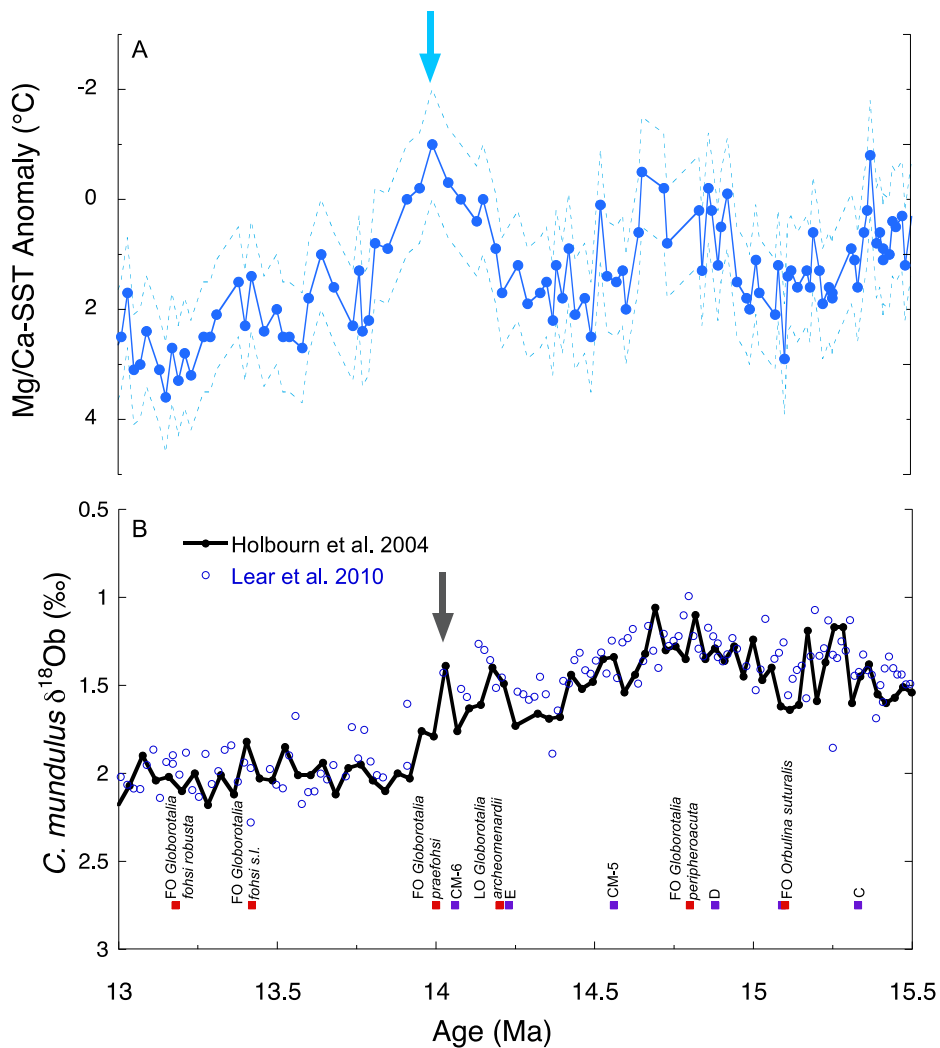
80
 81 **Figure S8** ODP site 761 Mg/Ca-SST reconstructions for a range of scenarios as follows (1)
 82 application of Gray and Evans (2019)(GE19) multi-variable regression accounting for
 83 changes in Mg/Ca_{sw}, (2) application of Anand et al., (2003) *T. sacculifer* Mg/Ca-T equation
 84 with Miocene Mg/Ca_{sw} value of 3.43 mmol/mol as estimated in Sosdian et al., (2020), and (3)
 85 application of Gray and Evans (2019) multi-variable regression with constant Miocene
 86 Mg/Ca_{sw} value of 3.43 mmol/mol.
 87



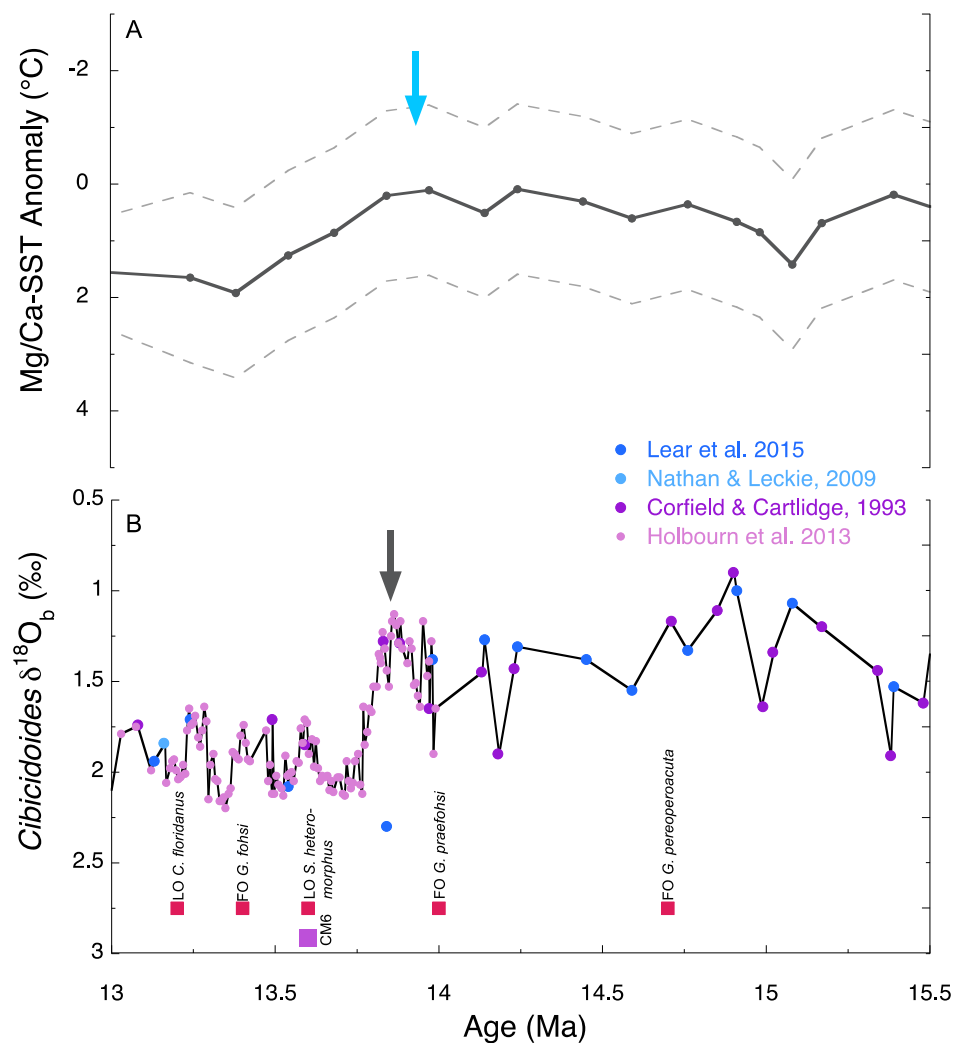
88
 89 **Figure S9** ODP site 1171 Mg/Ca-SST reconstructions derived from the sensitivity analysis
 90 (A) SST estimates derived from ODP site 1171 *G. bulloides* Mg/Ca with varying salinity
 91 scenarios (constant modern, constant modern +1 PSU, constant modern -1 PSU); (B) SST
 92 estimates derived using the Mg/Ca-T equation from Mashiotta et al., (1999) and assuming
 93 modern values for Mg/Ca_{sw} (Shevenell et al., 2004) and using Gray and Evans (2019) multi-
 94 variable regression accounting for changes in pH, salinity, and Mg/Ca_{sw}.
 95
 96



98
 99 **Figure S10** ODP Site 1171 (A) Mg/Ca-derived SST anomaly (calculated from record of
 100 Shevenell et al., (2004) and (B) benthic foraminiferal oxygen isotope records. Datums used in
 101 the age model are shown by colored squares (biostratigraphic datums-red squares, isotopic
 102 datums-purple squares, magnetostratigraphic datums-grey squares; Shevenell & Kennett,
 103 2004). Blue arrows show major cooling steps in the Southern Ocean (Shevenell et al., 2004).
 104 Initial surface cooling step follows CM-5, but precedes magnetostratigraphic datum C5ACn,
 105 isotope event CM6 and the glaciation step (grey arrow).

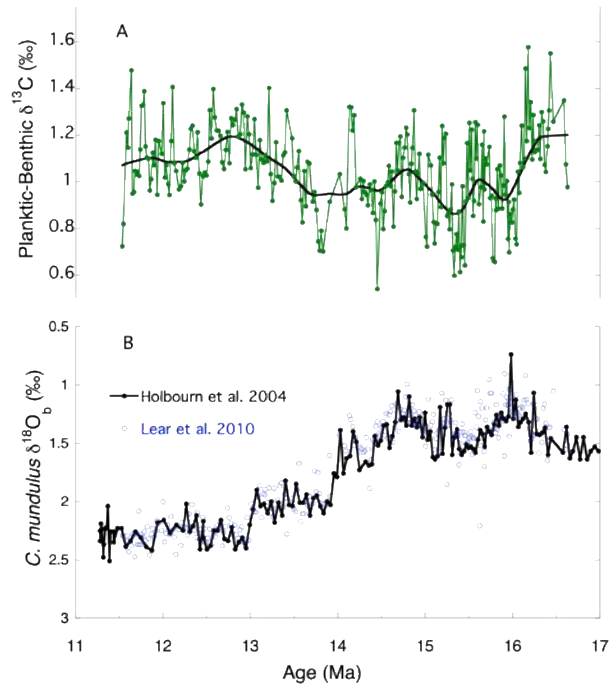


106
 107 **Figure S11** ODP Site 761 (A) Mg/Ca-derived SST anomaly (this study) and (B) benthic
 108 foraminiferal oxygen isotope records (Holbourn et al., 2004; Lear et al., 2010). Datums used
 109 in ODP Site 761 age model are shown by colored squares (biostratigraphic datums-red squares,
 110 isotopic datums-purple squares). Major MMCT surface cooling is shown by blue arrow, and
 111 occurs in step with CM6 and the main glaciation step (grey arrow).



112
 113 **Figure S12** ODP Site 806 (A) Mg/Ca-derived SST anomaly (this study) and (B) benthic
 114 foraminiferal oxygen isotope records (Corfield and Cartlidge, 1983; Nathan and Leckie, 2009;
 115 Holbourn et al., 2013; Lear et al., 2015). Datums used in ODP Site 806 age model are marked
 116 by colored squares (biostratigraphic datums-red squares, isotopic datums-purple squares,
 117 magnetostratigraphic datums-gray squares). Cooling (blue arrow) and glaciation step (grey
 118 arrow) are marked in each record. Note CM6 isotope datum was not used in Lear et al., (2015)
 119 age model.

120
 121
 122
 123
 124
 125
 126



127
 128
 129
 130
 131
 132

Figure S13 (A) $\delta^{13}\text{C}$ difference between planktonic (*T. trilobus*; Sosdian et al., 2020) and benthic foraminifera (*Cibicidoides sp.*; Holbourn et al., 2004; Lear et al., 2010) indicative of productivity at site 761 in the tropical Indian Ocean alongside the (b) compiled $\delta^{18}\text{O}_b$ records from ODP site 761 (Holbourn et al., 2004; Lear et al., 2004). Note more positive $\delta^{13}\text{C}$ values indicate more productivity.

133
134
135
136

Supplementary Tables

Supplementary Table S1 Datums used in Age Models for ODP Sites 761, 806 and 1171 across the Middle Miocene Climate Transition (13-15.5 Ma).

ODP site 761

Datum	Age (Ma)	Datum Type	Reference
FO <i>Globorotalia fohsi robusta</i>	13.18	Biostratigraphic	Holbourn et al. 2004
FO <i>Globorotalia fohsi s.l.</i>	13.42	Biostratigraphic	Holbourn et al. 2004
CM6	14.06	Isotopic	Holbourn et al. 2004
FO <i>Globorotalia praefohsi</i>	14	Biostratigraphic	Holbourn et al. 2004
LO <i>Globorotalia archeomenardii</i>	14.2	Biostratigraphic	Holbourn et al. 2004
E	14.23	Isotopic	Holbourn et al. 2004
CM5	14.56	Isotopic	Holbourn et al. 2004
D	14.88	Isotopic	Holbourn et al. 2004
FO <i>Globorotalia peripheroacuta</i>	14.8	Biostratigraphic	Holbourn et al. 2004
FO <i>Orbulina suturalis</i>	15.1	Biostratigraphic	Holbourn et al. 2004

ODP site 806

Datum	Age (Ma)	Datum Type	Reference
FO <i>G. fohsi</i>	13.4	Biostratigraphic	Lear et al. 2015
LO <i>C. floridanus</i>	13.2	Biostratigraphic	Lear et al. 2015
LO <i>S. heteromorphus</i>	13.6	Biostratigraphic	Lear et al. 2015
FO <i>G. praefohsi</i>	14.0	Biostratigraphic	Lear et al. 2015
FO <i>G. peripheroacuta</i>	14.7	Biostratigraphic	Lear et al. 2015

ODP site 1171

Datum	Age (Ma)	Datum Type	Reference
Top C5ABn	13.302	Magneto	Shevenell & Kennett, 2004
C5ABn	13.51	Magneto	Shevenell & Kennett, 2004
CM6	13.6	Isotopic	Shevenell & Kennett, 2004
Top C5ACn	13.703	Magneto	Shevenell & Kennett, 2004
C5ACn	14.076	Magneto	Shevenell & Kennett, 2004
CM5	14.46	Isotopic	Shevenell & Kennett, 2004
FO <i>Orbulina suturalis</i> (F)	15.1	Biostratigraphic	Shevenell & Kennett, 2004

137
138
139

Supplementary Table S2 *D. Altispira* Mg/Ca and oxygen isotope data at ODP site 806.

Site-Hole	Core	Sect	Interval (cm)		Depth (MCD)	Age (Ma)	Mg/Ca (mmol/mol)	<i>D. altispira</i> $\delta^{18}\text{O}$ (‰)
806B	43	2	80	85	399.8	11.3	3.64	-0.73
806B	44	2	83	87	409.52	11.6	3.44	-0.89
806B	44	5	93	95	414.13	11.7	3.83	-0.76
806B	44	6	113.5	115.5	415.835	11.8	3.72	-0.78
806B	45	2	92	97	419.32	11.9	3.50	-0.78
806B	45	3	76	78	420.66	11.9	3.54	-0.90
806 B	45	5	81	86	423.71	12.0	3.66	-0.91
806B	45	6	108.5	110.5	425.485	12.0	3.55	-0.96
806 B	46	2	82	87	428.82	12.1	3.48	-0.68
806B	46	5	82	87	433.32	12.3	3.47	-0.84

806 B	47	2	70	76	438.3	12.4	3.31	-0.66
806 B	47	5	38	43	442.48	12.5	3.65	-0.50
806 B	48	2	64	69	447.94	12.7	3.29	-1.06
806 B	48	5	60	65	452.4	12.8	3.41	-0.74
806B	49	2	68	73	457.68	13.0	3.37	-0.73
806 B	50	2	70	75	465.8	13.2	3.33	-0.95
806B	50	5	80	85	470.4	13.4	3.25	-1.05
806 B	51	2	68	73	475.48	13.5	3.44	-0.78
806 B	51	5	80	85	480.1	13.7	3.56	-0.70
806 B	52	2	88	93	484.98	13.8	3.77	-1.29
806 B	52	5	77	82	489.37	14.0	3.80	-0.94
806 B	53	2	71	76	494.51	14.1	3.66	-1.04
806 B	53	4	80	85	497.6	14.2	3.79	-1.02
806 B	54	2	71	76	504.11	14.4	3.71	-0.97
806 B	54	5	66	68	508.56	14.6	3.61	-0.92
806 B	55	2	80	85	513.9	14.8	3.68	-1.05
806 B	55	5	102	104	518.4	14.9	3.58	-1.02
806B	55	7	19	21	520.79	15.0	3.51	
806 B	56	2	87	92	523.67	15.1	3.34	-1.29
806 B	56	4	69	74	526.49	15.2	3.56	-1.48
806 B	57	2	70	75	533.1	15.4	3.71	-0.93
806 B	57	5	80	85	537.7	15.5	3.61	-0.79

806 B	58	2	70	75	542.7	15.7	3.86	-0.82
806 B	58	5	75	80	547.25	15.9	3.72	-1.26
806 B	59	2	70	75	552.4	16.0	3.87	-0.72
806 B	59	5	80	85	557	16.2	3.88	-1.09
806 B	60	2	80	85	562.2	16.3	3.74	-0.83
806 B	60	5	36	41	566.26	16.5	3.45	-1.24

140

141

Supplementary Table S3 *T. trilobus* oxygen isotope data at ODP site 761.

Site- Hole	Core	Section	Interval (cm)	MBSF	MCD	Age (Ma)	<i>T. trilobus</i> $\delta^{18}\text{O}$ (‰)
761B	5	2	88-90	35.08	35.58	11.55	-0.96
761B	5	2	103-105	35.23	35.73	11.59	-0.94
761B	5	2	108-110	35.28	35.78	11.60	-0.86
761B	5	2	113-115	35.33	35.83	11.61	-0.88
761B	5	2	123-125	35.43	35.93	11.64	-0.94
761B	5	2	128-130	35.48	35.98	11.65	-0.93
761B	5	2	138-140	35.58	36.08	11.68	-1.04
761B	5	2	148-150	35.68	36.18	11.71	-1.27
761B	5	3	3-5	35.73	36.23	11.73	-0.99
761B	5	3	8-10	35.78	36.28	11.74	-1.07
761B	5	3	13-15	35.83	36.33	11.76	-1.08
761B	5	3	18-20	35.88	36.38	11.77	-1.03
761B	5	3	23-25	35.93	36.43	11.79	-1.05

761B	5	3	33-35	36.03	36.53	11.82	-0.96
761B	5	3	38-40	36.08	36.58	11.84	-0.95
761B	5	3	43-45	36.13	36.63	11.85	-0.99
761B	5	3	53-55	36.23	36.73	11.88	-0.80
761B	5	3	58-60	36.28	36.78	11.90	-1.36
761B	5	3	63-65	36.33	36.83	11.92	-0.87
761B	5	3	68-70	36.38	36.88	11.94	-0.97
761B	5	3	73-75	36.43	36.93	11.95	-0.87
761B	5	3	78-80	36.48	36.98	11.97	-0.82
761B	5	3	88-90	36.58	37.08	12.00	-0.70
761B	5	3	93-95	36.63	37.13	12.02	-0.99
761B	5	3	98-100	36.68	37.18	12.04	-1.45
761B	5	3	103-105	36.73	37.23	12.06	-0.87
761B	5	3	108-110	36.78	37.28	12.08	-0.81
761B	5	3	118-120	36.88	37.38	12.11	-0.80
761B	5	3	123-125	36.93	37.43	12.13	-1.06
761B	5	3	128-130	36.98	37.48	12.15	-0.87
761B	5	3	138-140	37.08	37.58	12.19	-0.80
761B	5	3	148-150	37.18	37.68	12.22	-1.06
761B	5	4	3-5	37.23	37.73	12.24	-0.85
761B	5	4	8-10	37.28	37.78	12.26	-0.92
761B	5	4	13-15	37.33	37.83	12.28	-1.00
761B	5	4	18-20	37.38	37.88	12.30	-0.89
761B	5	4	28-30	37.48	37.98	12.34	-0.81
761B	5	4	38-40	37.58	38.08	12.38	-0.78

761B	5	4	43-45	37.63	38.13	12.40	-0.81
761B	5	4	48-50	37.68	38.18	12.42	-0.98
761B	5	4	58-60	37.78	38.28	12.46	-1.05
761B	5	4	63-65	37.83	38.33	12.48	-0.88
761B	5	4	68-70	37.88	38.38	12.50	-0.70
761B	5	4	88-90	38.08	38.58	12.58	-0.90
761B	5	4	98-100	38.18	38.68	12.62	-0.72
761B	5	4	103-105	38.23	38.73	12.64	-0.78
761B	5	4	113-115	38.33	38.83	12.68	-0.67
761B	5	4	118-120	38.38	38.88	12.70	-0.74
761B	5	4	128-130	38.48	38.98	12.74	-0.75
761B	5	4	138-140	38.58	39.08	12.78	-0.66
761B	5	4	143-145	38.63	39.13	12.80	-0.80
761B	5	4	148-150	38.68	39.18	12.82	-0.62
761B	5	5	3-5	38.73	39.23	12.84	-0.83
761B	5	5	8-10	38.78	39.28	12.86	-0.69
761B	5	5	18-20	38.88	39.38	12.90	-0.75
761B	5	5	23-25	38.93	39.43	12.92	-1.01
761B	5	5	28-30	38.98	39.48	12.95	-0.79
761B	5	5	33-35	39.03	39.53	12.97	-0.92
761B	5	5	43-45	39.13	39.63	13.01	-0.80
761B	5	5	48-50	39.18	39.68	13.03	-0.96
761B	5	5	53-55	39.23	39.73	13.05	-0.73
761B	5	5	58-60	39.28	39.78	13.07	-0.92
761B	5	5	63-65	39.33	39.83	13.09	-0.89

761B	5	5	73-75	39.43	39.93	13.13	-0.99
761B	5	5	78-80	39.48	39.98	13.15	-1.22
761B	5	5	83-85	39.53	40.03	13.17	-0.90
761B	5	5	88-90	39.58	40.08	13.19	-1.05
761B	5	5	93-95	39.63	40.13	13.21	-1.11
761B	5	5	98-100	39.68	40.18	13.23	-0.98
761B	5	5	108-110	39.78	40.28	13.27	-1.23
761B	5	5	113-115	39.83	40.33	13.29	-1.20
761B	5	5	118-120	39.88	40.38	13.32	-1.10
761B	5	5	133-135	40.03	40.53	13.38	-1.45
761B	5	5	138-140	40.08	40.58	13.40	-0.82
761B	5	5	143-145	40.13	40.63	13.42	-0.77
761B	5	6	3-5	40.23	40.73	13.46	-0.70
761B	5	6	18-20	40.38	40.88	13.52	-1.05
761B	5	6	23-25	40.43	40.93	13.54	-1.07
761B	5	6	28-30	40.48	40.98	13.56	-0.57
761B	5	6	38-40	40.58	41.08	13.60	-0.76
761B	5	6	43-45	40.63	41.13	13.62	-0.89
761B	5	6	48-50	40.68	41.18	13.64	-0.87
761B	5	6	58-60	40.78	41.28	13.68	-0.96
761B	5	6	73-75	40.93	41.43	13.74	-0.80
761B	5	6	78-80	40.98	41.48	13.76	-0.73
761B	5	6	83-85	41.03	41.53	13.78	-0.49
761B	5	6	93-95	41.13	41.63	13.81	-0.70
761B	5	6	113-115	41.23	41.73	13.85	-0.39

761B	5	6	118-120	41.38	41.88	13.91	-0.41
761B	5	6	128-130	41.48	41.98	13.95	-0.53
761B	5	6	138-140	41.58	42.08	13.99	-0.70
761B	5	7	3-5	41.73	42.23	14.04	-0.60
761B	5	7	13-15	41.83	42.33	14.08	-1.17
761B	5	7	28-30	41.98	42.48	14.13	-1.25
761B	5	CC	8-10	42.32	42.82	14.26	-1.05
761B	5	CC	18-20	42.42	42.92	14.29	-0.97
761B	5	CC	28-30	42.52	43.02	14.33	-0.94
761B	5	CC	33-35	42.57	43.07	14.35	-1.13
761B	6	1	3-5	42.23	43.13	14.37	-0.64
761B	6	1	8-10	42.28	43.18	14.38	-1.04
761B	6	1	13-15	42.33	43.23	14.40	-0.81
761B	6	1	18-20	42.38	43.28	14.42	-0.60
761B	6	1	23-25	42.43	43.33	14.44	-0.85
761B	6	1	38-40	42.58	43.48	14.49	-0.97
761B	6	1	48-50	42.68	43.58	14.52	-0.93
761B	6	1	53-55	42.73	43.63	14.54	-0.76
761B	6	1	63-65	42.83	43.73	14.57	-1.03
761B	6	1	68-70	42.88	43.78	14.59	-0.88
761B	6	1	73-75	42.93	43.83	14.60	-0.93
761B	6	1	78-80	42.98	43.88	14.62	-0.86
761B	6	1	83-85	43.03	43.93	14.64	-0.98
761B	6	1	88-90	43.08	43.98	14.65	-0.59
761B	6	1	98-100	43.18	44.08	14.69	-1.02

761B	6	1	103-105	43.23	44.13	14.70	-0.65
761B	6	1	108-110	43.28	44.18	14.72	-0.80
761B	6	1	113-115	43.33	44.23	14.73	-0.72
761B	6	1	118-120	43.38	44.28	14.75	-0.73
761B	6	1	123-125	43.43	44.33	14.77	-0.90
761B	6	1	128-130	43.48	44.38	14.78	-0.35
761B	6	1	138-140	43.58	44.48	14.81	-0.74
761B	6	1	143-145	43.63	44.53	14.83	-1.29
761B	6	1	148-150	43.68	44.58	14.84	-0.70
761B	6	2	3-5	43.73	44.63	14.86	-0.84
761B	6	2	8-10	43.78	44.68	14.87	-0.75
761B	6	2	13-15	43.83	44.73	14.89	-0.74
761B	6	2	18-20	43.88	44.78	14.90	-1.14
761B	6	2	23-25	43.93	44.83	14.92	-0.83
761B	6	2	33-35	44.03	44.93	14.95	-0.85
761B	6	2	43-45	44.13	45.03	14.98	-0.97
761B	6	2	48-50	44.18	45.08	14.99	-1.00
761B	6	2	53-55	44.23	45.13	15.01	-0.87
761B	6	2	58-60	44.28	45.18	15.02	-0.79
761B	6	2	73-75	44.43	45.33	15.07	-0.96
761B	6	2	78-80	44.48	45.38	15.08	-0.97
761B	6	2	83-85	44.53	45.43	15.10	-1.02
761B	6	2	88-90	44.58	45.48	15.11	-0.97
761B	6	2	93-95	44.63	45.53	15.12	-0.67
761B	6	2	98-100	44.68	45.58	15.14	-0.26

761B	6	2	108-110	44.78	45.68	15.17	-0.91
761B	6	2	113-115	44.83	45.73	15.18	-0.76
761B	6	2	118-120	44.88	45.78	15.19	-0.70
761B	6	2	123-125	44.93	45.83	15.21	-0.52
761B	6	2	128-130	44.98	45.88	15.22	-0.77
761B	6	2	133-135	45.03	45.93	15.24	-0.75
761B	6	2	138-140	45.08	45.98	15.25	-0.70
761B	6	2	138-140	45.08	45.98	15.25	-0.70
761B	6	3	13-15	45.33	46.23	15.32	-0.56
761B	6	3	28-30	45.48	46.38	15.36	-0.67
761B	6	3	33-35	45.53	46.43	15.37	-0.70
761B	6	3	38-40	45.58	46.48	15.39	-0.62
761B	6	3	43-45	45.63	46.53	15.40	-0.37
761B	6	3	46-48	45.66	46.56	15.41	-0.78
761B	6	3	48-50	45.68	46.58	15.41	-0.66
761B	6	3	53-55	45.73	46.63	15.43	-0.37
761B	6	3	58-60	45.78	46.68	15.44	-0.13
761B	6	3	63-65	45.83	46.73	15.45	-0.36
761B	6	3	68-70	45.88	46.78	15.47	-0.52
761B	6	3	73-75	45.93	46.83	15.48	-0.47
761B	6	3	83-85	46.03	46.93	15.51	-0.40
761B	6	3	88-90	46.08	46.98	15.52	-0.53
761B	6	3	93-95	46.13	47.03	15.53	-0.42
761B	6	3	98-100	46.18	47.08	15.55	-0.34
761B	6	3	103-105	46.23	47.13	15.56	-0.57

761B	6	3	108-110	46.28	47.18	15.57	-0.20
761B	6	3	113-115	46.33	47.23	15.59	-0.32
761B	6	3	133-135	46.53	47.43	15.64	-0.43
761B	6	3	143-145	46.63	47.53	15.67	-0.50
761B	6	3	148-150	46.68	47.58	15.68	-0.22
761B	6	4	38-40	47.08	47.98	15.79	-0.69
761B	6	4	43-45	47.13	48.03	15.80	-0.52
761B	6	4	53-55	47.23	48.13	15.83	-0.45
761B	6	4	63-65	47.33	48.23	15.85	-0.74
761B	6	4	68-70	47.38	48.28	15.87	-0.41
761B	6	4	73-75	47.43	48.33	15.88	-0.35
761B	6	4	83-85	47.53	48.43	15.91	-0.41
761B	6	4	98-100	47.68	48.58	15.95	-0.31
761B	6	4	118-120	47.88	48.78	16.00	-0.45
761B	6	4	123-125	47.93	48.83	16.02	-0.34
761B	6	4	128-130	47.98	48.88	16.03	-0.37
761B	6	4	146-148	48.16	49.06	16.08	-0.43
761B	6	4	148-150	48.18	49.08	16.09	-0.39
761B	6	5	3-5	48.23	49.13	16.10	-0.52
761B	6	5	23-25	48.43	49.33	16.16	-0.65
761B	6	5	33-35	48.53	49.43	16.19	-0.49
761B	6	5	43-45	48.63	49.53	16.22	-0.58
761B	6	5	50-52	48.7	49.6	16.25	-0.52
761B	6	5	63-65	48.83	49.73	16.29	-0.60
761B	6	5	73-75	48.93	49.83	16.32	-0.52

761B	6	5	83-85	49.03	49.93	16.35	-0.44
761B	6	5	93-95	49.13	50.03	16.38	-0.25
761B	6	5	100-102	49.2	50.1	16.41	-0.45
761B	6	5	108-110	49.28	50.18	16.43	-0.29

142
143
144
145
146
147
148
149
150
151
152
153
154
155
156
157
158
159
160
161
162
163
164
165
166
167

168
169
170
171
172
173
174
175
176
177
178
179
180
181
182
183